CHAPTER 4. ELECTROCATALYTIC OXIDATION OF HCOOH ON A Pt RING ELECTRODE

4.1 Introduction

The occurrence of temporally self-organised dynamical states immediately raises the question of spontaneously generated spatial inhomogeneities in the catalytic activity of the electrode. Obviously, studying the relation between the integral temporal behaviour and the corresponding spatial distribution of the interfacial potential, that is the local profile of the electrocatalytic activity, is important for the understanding of electrochemical instabilities. Thus, while earlier studies evidenced pattern formation of inhomogeneous *interfacial potential* in electrodissolution reactions [12, 14 – 17], the research has been recently addressing pattern formations in **electrocatalysis** [19, 21 – 24, 122]. Detailed theoretical descriptions of spatiotemporal electrochemical patterns provided valuable guidance for the understanding of spatiotemporal instability.

The electrocatalytic oxidation of HCOOH on Pt in the presence of foreign adatoms to be explained in this chapter is one of the most studied subjects experimentally and theoretically in electrocatalysis of organic oxidations [123]. This reaction may be considered as a model to understand the oxidation of more complex organic species (*e.g.*, methanol) on a Pt electrode, since it produces carbon dioxide and interfacial electrons that are of great interest in direct fuel cell applications.

In this chapter, after a short outline of the mechanistic origin of current oscillations in the electrocatalytic oxidation of formic acid (HCOOH) on a Pt electrode modified by Bi deposition (see section 4.3), the investigation of spatiotemporal patterns in the interfacial potentials corresponding to temporal oscillatory behaviours will be followed. System parameters such as applied potential or mass-transport conditions could induce the primary interest of the distribution of interfacial potential along the ring-shaped media (see section 4.4). We then explain experiments and computer

simulations of an electrochemical system where the direction of a pulse can be reversed at will using an external perturbation (section 4.5). In section 4.6, the influence of the position of the reference electrode is studied, since the dynamics and patterns often are a result of the interaction of reaction kinetics and the potential drop through the electrolyte. Finally, some spatiotemporal mixed-mode oscillations (SMMOs) are briefly described in section 4.7.

4.2 Experimental procedure

Electrochemical setup

Figure 4.1 shows the schematic experimental setup for monitoring of the local potential distributions at electrochemical interfaces studied. The electrochemical cell body consisted of a glass cylinder capped with a Teflon lid holding all electrodes. A smooth polycrystalline Pt ring with inner diameter of 34.5 mm and with outer diameter of 40.5 mm (thickness of 0.1 mm) was used as working electrode (WE). The geometric area of the WE was $7\,cm^2$. A concentric platinized Pt wire ring of 70 mm diameter (1 mm wire thickness) was used as counter electrode (CE). The tip of a Luggin-Haber capillary hosting a Hg/Hg_2SO_4, saturated K_2SO_4 reference electrode (RE) was placed in the centre of the ring WE. Unless stated otherwise, experiments have been performed in the absence of forced convection such as magnetic stirring or gas (*e.g.*, nitrogen) bubbling.

A home-built potentiostat/scan generator (*ELAB* of Fritz-Haber-Institut) was used for all cyclic voltammetry (CV) and chronoamperometry (CA) experiments and the data were transferred to an IBM compatible PC controlled by a GPIB interface. Galvanostatic experiments were performed by means of a bi-potentiostat (EG&G, Model 366).

Solutions and electrode treatment

All solutions were prepared with ultrapure water (Millipore Milli–Q water, $18\ M\Omega \cdot cm$). Prior to the experiment, the Pt ring WE was first subjected to cleaning

with acetone and pure water in an ultrasonic bath followed by chemical cleaning in a mixture of conc. H_2SO_4 (Merck, suprapur) : 30 % H_2O_2 (1 : 1).

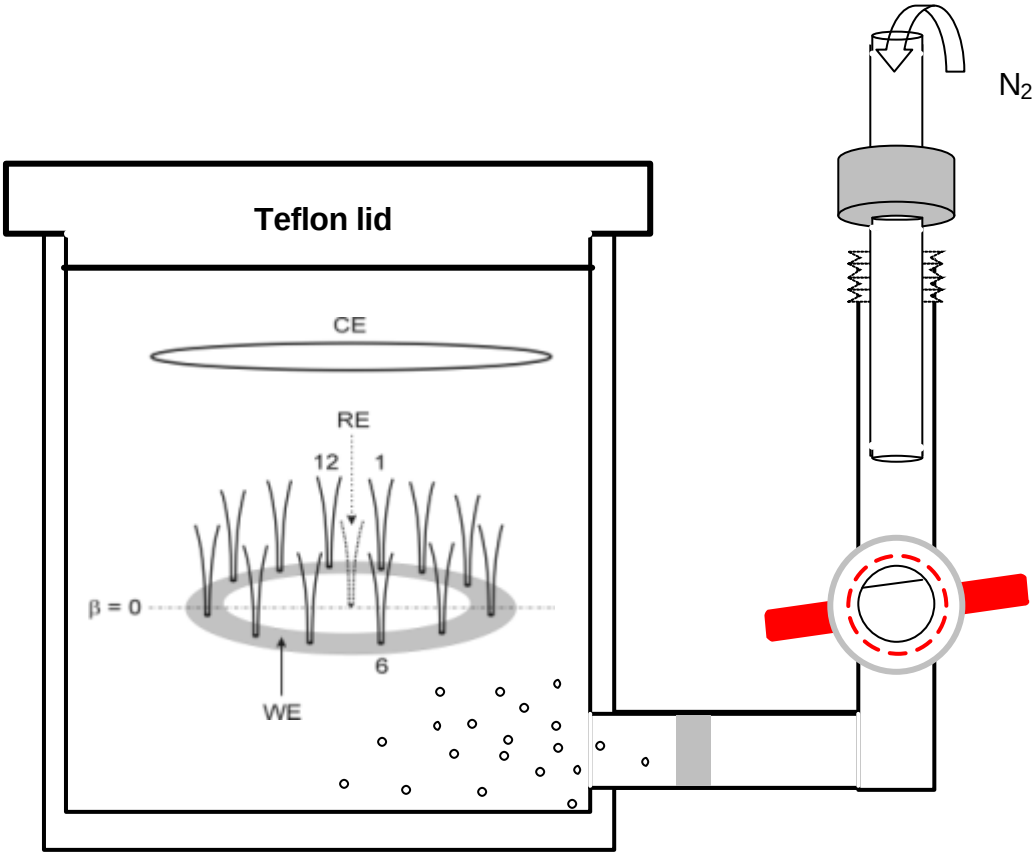

Figure 4.1. Schematic diagram of experimental setup for the measurements of HCOOH oxidation on a Pt ring electrode.

Figure 4.2 shows a preliminary check of the voltammetric curve between – 600 mV and + 800 mV of the WE performed in 0.5 M H_2SO_4 deaerated by high-purity N_2 (99.999 %) to verify the absence of any residuals of impurities. One can clearly see that there are two peak pairs of adsorption/desorption of hydrogen in the potential range between – 400 mV and – 600 mV. A well-defined peak pair of oxidation/reduction of Pt electrode marked with I and I' around + 100 mV ~ + 200 mV is also found. This result indicates that polycrystalline Pt electrode used in this work has a smooth and clean surface. For all experiments involving formic acid oxidation, a deaerated solution mixture of 0.1 M HCOONa (Merck, p.a.) and 0.033 M H_2SO_4 (Merck, suprapur) was

employed as the electrolyte. The formic acid buffer solution has a constant bulk pH value of 2.85 and a resistivity of $107\,\Omega \cdot \mathrm{cm}$. After the experiments, the WE was treated in conc. $HClO_4$ (Merck, suprapur) and conc. HNO_3 (Merck, suprapur) in order to completely remove Bi complex residuals.

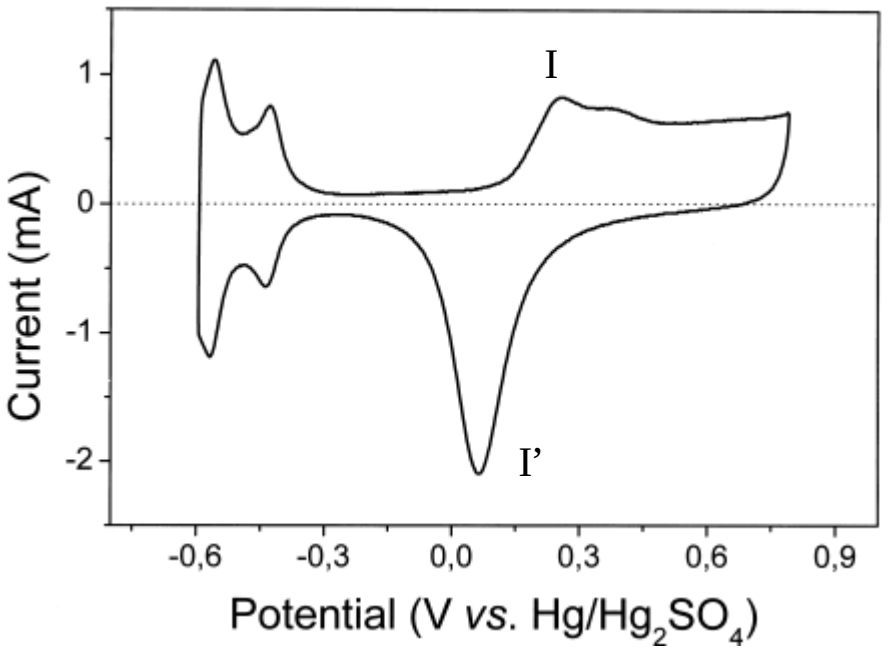

Figure 4.2. Cyclic voltammetry in 0.5 M H_2SO_4 on a smooth Pt electrode with a scan rate of 100 mV/s.

Bi modifications

Unlike most other studies of formic acid oxidation on Bi-modified electrodes, Bi deposition modifications of the Pt WE in this work was done with under potential deposition (UPD) of Bi. In other words, Bi ions were present in the bulk electrolyte throughout the entire experiment. A 1×10^{-3} M Bi^{3+} containing solution was prepared by dissolution of high-purity Bi (III) oxide (Bi_2O_3, Strem Chemicals Inc., 99.9998 %) in 0.5 M $HClO_4$ (Merck, suprapur). Appropriate amounts of the 1×10^{-3} M Bi^{3+} solution were added to the electrolyte to obtain final concentrations of Bi^{3+} ranging from 1×10^{-5} M to 1×10^{-7} M. After adding Bi ions into the electrolyte and prior to each cyclic voltammetry, the initial WE potential was kept at its open circuit potential (OCP,

– 320 mV *vs.* Hg/Hg_2SO_4) for 3 min in order to establish the same Bi coverage on the Pt electrode.

Figure 4.3 shows the surface morphology of the Pt surface after Bi modification. Round-shaped clusters were observed on the Pt surface. Magnification is × 25,000 and the size of the single deposited Bi cluster is about 70 nm (see dotted circle). This cluster is clearly ascribed to Bi by means of electron dispersive spectroscopy (EDX) analysis (Figure 4.4).

Figure 4.3. SEM image of a Bi deposited Pt surface.

Electrochemical Impedance Spectroscopy (EIS)

Impedance spectra were measured at various constant outer potentials using a potentiostat & galvanostat (EG&G, PAR 273A)/log-in amplifier (NF Circuit design Block Co., Frequency response analyser, Model S-5720) setup attached to the electrochemical cell described earlier [124, 125]. The desired outer applied potentials were adjusted during the anodic voltammetric scan, and then the system was allowed to settle to stationary mass-transport conditions. Between two successive measurements, the electrode potential was scanned once between + 250 mV and – 500 mV to ensure comparable surface conditions (see the following section 4.3). The frequency range investigated reached from 10 kHz to 0.1 Hz with 25 points per decade (*e.g.*, 10 Hz to 100 Hz or 1 kHz to 100 kHz).

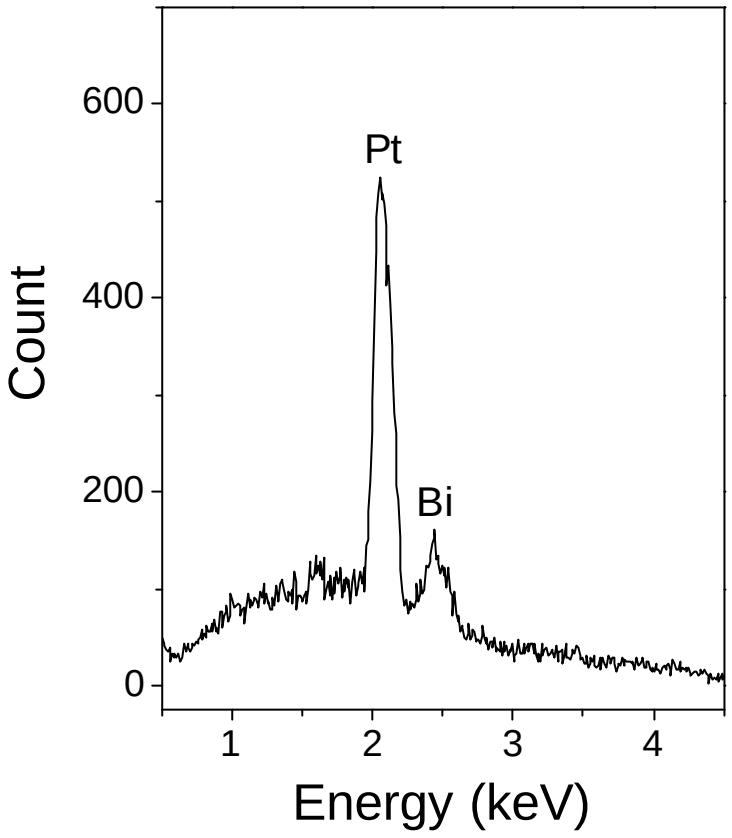

Figure 4.4. EDX data of a Bi deposited Pt surface.

Rotating Ring Disc Electrode (RRDE)

For the *in-situ* characterisation of the adsorption/desorption of reducible species, rotating ring disc electrode (RRDE, Tacussel electronique) measurements were performed. Both disc and ring are polycrystalline Pt. The geometric surface areas of ring and disc were 0.1254 cm^2 and 0.2827 cm^2, respectively. A Pt coil and a Hg/Hg_2SO_4 electrode served as counter electrode and reference electrode, respectively. Figure 4.5 is the schematic diagram of the RRDE cell. In the RRDE experiment, the Pt ring electrode was kept at -580 mV with the disc rotation set to 2000 rpm. The reported RRDE measurements plot the instantaneous deviation ΔI_{ring} of the stationary ring current I_{ring}^{0} versus potential.

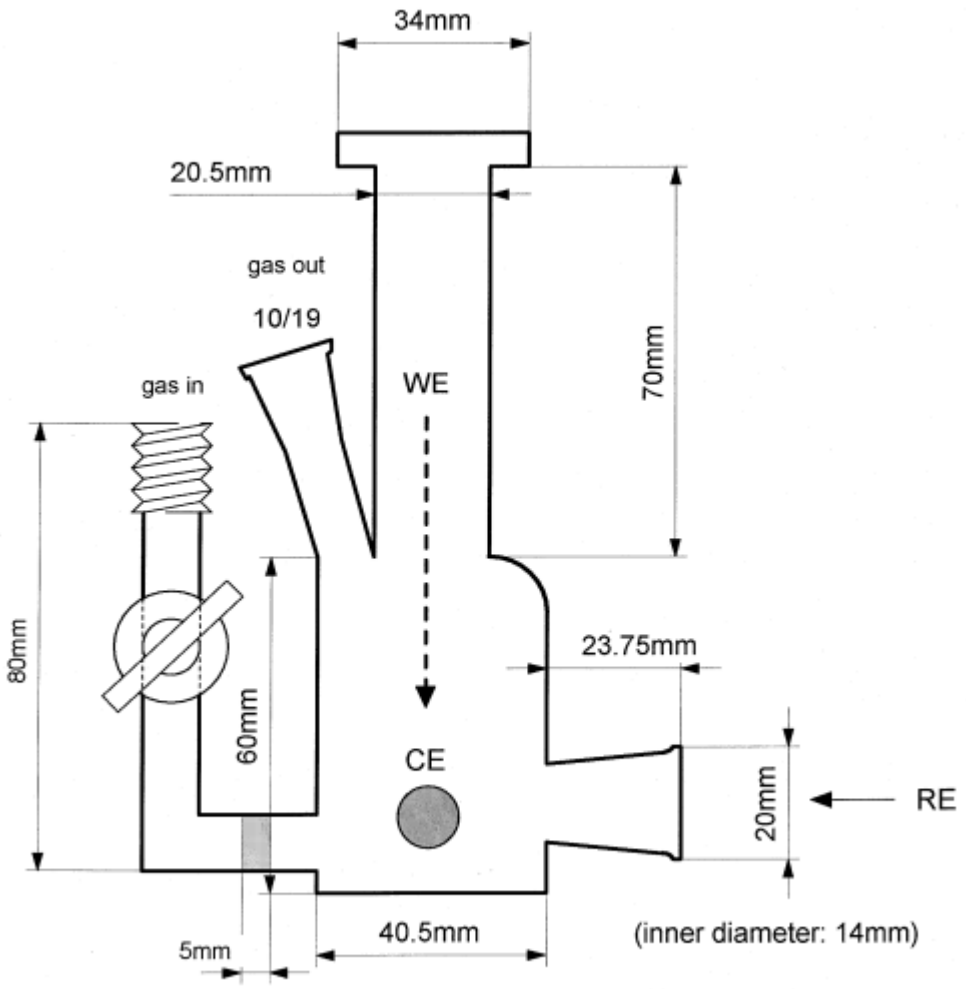

Figure 4.5. Schematic diagram of the experimental setup for rotating ring disc (RRDE) electrode measurements.

Apiezon Wax Coating

In order to avoid an additional effect of inhomogeneous electrical supply to the Pt ring working electrode during the measurement of interfacial potential with microprobes, Apiezon wax was used to coat the connecting part between ring electrode and working electrode wire encapsulated by glass. Apiezon has been usually used for the preparation of the tungsten tip of the electrochemical scanning tunnelling microscope (EC-STM) (see following Figure 4.6 for detailed coating process).

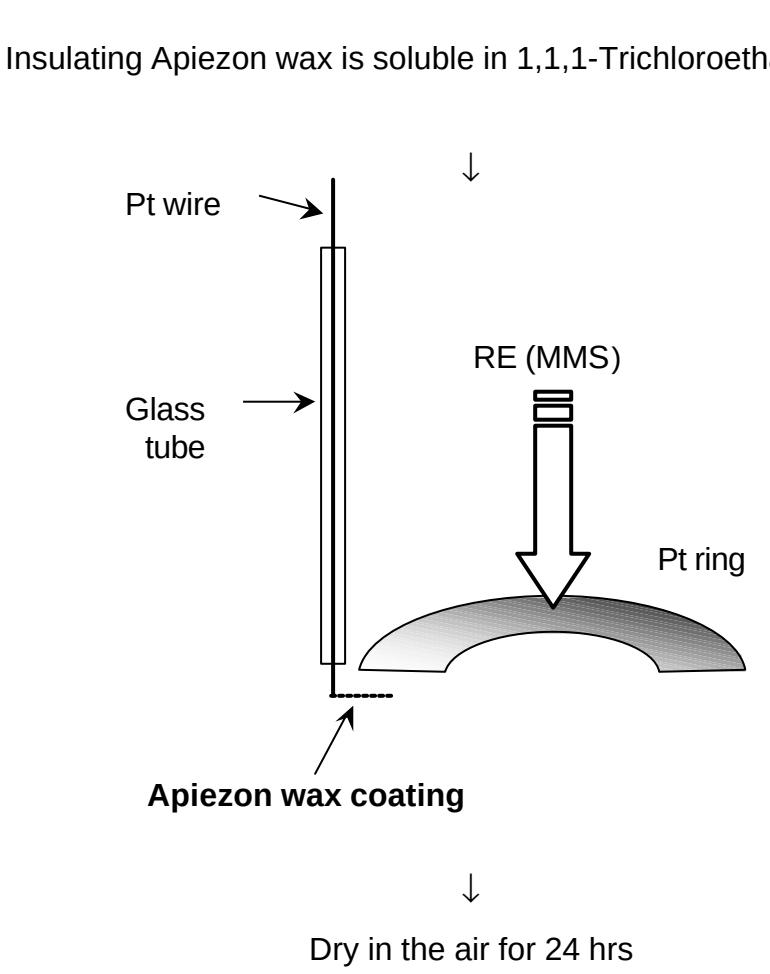

Figure 4.6. Three steps of coating process of insulating Apiezon wax.

4.3 On the origin of oscillations in the electrocatalytic oxidation of HCOOH on a Pt electrode modified by Bi deposition

Experimental observations on the temporal dynamics in the electrocatalytic oxidation of formic acid (HCOOH) on a polycrystalline Pt electrode modified by deposition of Bi are reported. Bi modification significantly enhanced the current density of HCOOH oxidation, since it suppressed the poisoning branch and increased the apparent direct oxidation rate. Impedance spectroscopy and the galvanostatic scan in HCOOH oxidation on Bi/Pt exhibited a hidden negative differential resistance and a Hopf bifurcation.

4.3.1 The study of underpotential deposition of Bi on Pt

The effect of underpotential deposition of Bi during cyclic voltammetry (CV) of the Pt electrode in 0.5 M H_2SO_4 is shown in Figure 4.7. CV (Figure 4.7(b)) in a solution containing 1×10^{-5} M Bi (III) shows that a high coverage of adsorbed Bi suppresses the adsorption of hydrogen [126]. Comparing with CV on pure Pt (see Figure 4.7(a)), several new voltammetric features on Bi-deposited Pt are obtained in the potential range between – 200 mV and + 400 mV. First of all, an asymmetric pair of oxidation peak I at + 200 mV on the anodic scan and of reduction peak I’ at + 100 mV on the cathodic scan is obtained. This result indicates that the formation and the reduction of Bi-oxygen species are considerably enhanced in the presence of Bi. A plateau marked with II is also obtained on the anodic scan. Secondly, we observe a weaker reversible redox process at III and III’ discernible around – 50 mV. The overall cyclic voltammetric profile on the Bi-modified Pt electrode qualitatively resembles a superposition of earlier current-potential curves obtained on Pt (100) and Pt (110) single crystals during Bi underpotential deposition [127, 128].

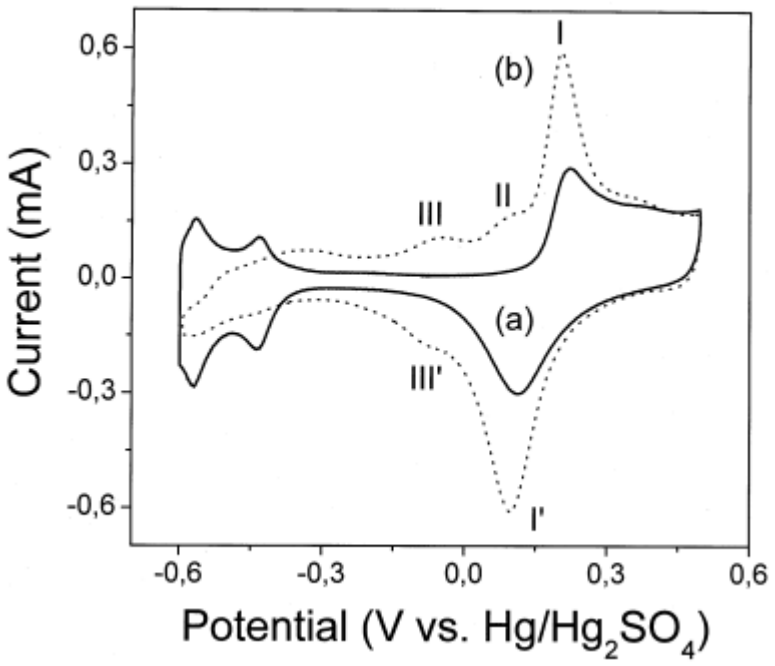

Figure 4.7. Cyclic voltammetry of a Pt working electrode with scan rate of 50 mV/s in the presence of Bi ion. (a) Solid line is the CV without Bi^{3+} and (b) dotted line presents the CV in 0.5 M H_2SO_4 with 1×10^{-5} M Bi^{3+}.

To investigate the adsorption/desorption behaviour of the Bi oxide species in detail, RRDE measurements of CV on Bi-modified Pt were carried out. Anodic redox peaks in the potential range of peaks I to III are commonly associated with a stepwise oxidation of adsorbed Bi adlayers by dissociative adsorption of water [127, 129, 130]. The ring potential was fixed at -580 mV to ensure the reduction of the dissolved Bi species and to avoid the evolution of hydrogen. Thus, the ring current is a measure of the local Bi (III) concentration. At pH = 0 (Figure 4.8(a)), the anodic profile of the disc current (except for peak III) matches the ring profile, indicating the formation of soluble Bi species at peaks I and II. Adsorbed metallic Bi is most likely oxidised to species such as Bi^{3+}, $Bi(OH)_2^{+}$, or $Bi(OH)^{2+}$. Peak III does not have any noticeable effect on the ring signal, suggesting that adsorbed metallic Bi is not directly involved in the redox process or the Bi species formed are insoluble. The cathodic ring signal in Figure 4.8(a) reveals reductive Bi adsorption between $+200$ mV (I') and -350 mV (III'). Note that the underpotential deposition technique causes the formation of dense or even multiple Bi adlayers by continuous adsorption of Bi during successive voltammetric cycles. In

other words, potential controlled deposition yields higher coverages than achievable under open-circuit operation. For a better understanding of the adsorption/desorption behaviour of Bi ions in HCOOH oxidation at pH = 2.85, we measured the CV in 0.5 M H_2SO_4 adjusted with NaOH to higher pH.

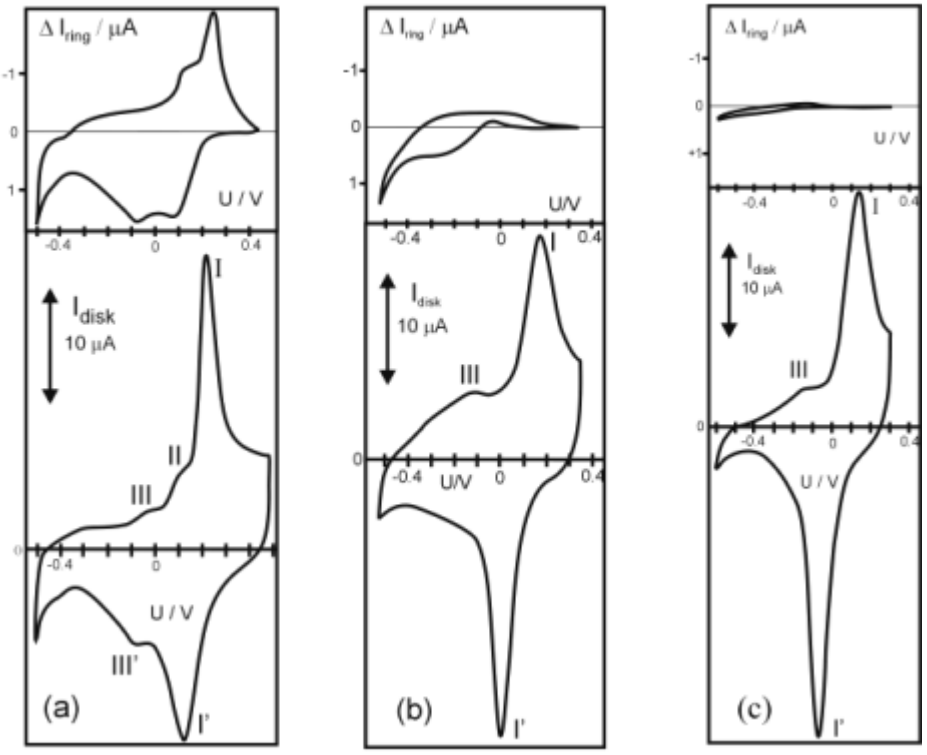

Figure 4.8. Rotating ring disc electrode (RRDE) analysis of Pt modified by Bi addition with scan rate of 50 mV/s. (a) pH = 0 (0.5 M H_2SO_4), (b) pH = 2 and (c) pH = 3. The concentration of Bi^{3+} is 5×10^{-5} M. The ring current is proportional to the deviation of the Bi ion concentration from this value.

At pH = 2 and pH = 3 (Figures 4.8(b) and 4.8(c)), the voltammetric ring profile has drastically changed compared with Figure 4.8(a). Despite comparable disc currents, both cathodic and anodic currents at the ring decrease dramatically. Thus, at peaks II and I there is very little dissolution of Bi at pH = 3. Obviously, Bi adlayers at peak III in Figure 4.8(b) transformed into Bi surface oxides with a much lower dissolution rate compared with the soluble Bi (III) species formed at pH = 0 (see Figure 4.8(a)). In Figure 4.8(b), only a small fraction of the Bi adlayers is dissolved near peak II, which largely coincides with peak I (– 100 mV to 0 mV in Figure 4.8(b)) for the Pt disc

employed. Although this result confirms that Bi redox processes around peak III are not associated with the formation of any soluble and reducible Bi species, the exact nature and oxidation state of the resulting Bi species is not clear.

The above experiments on Bi underpotential deposition reflect the following three distinct redox processes: (a) the increment of charge of peaks I and I' compared with pure Pt electrode involves the surface oxidation of the electrode; (b) a cathodic plateau prior to peak I, referred to as peak II; and (c) a relatively weaker and reversible pair of peaks III and III' is formed. The overall voltammetric profile of the above three processes on the electrode is in good agreement with the behaviour of Pt (100) or Pt (110) single crystals [127, 128]. Although the Pt (111) surface is known to exhibit a single sharp redox feature around peaks III/III' [127, 128, 130], its contribution may be small, based on the relative peak heights.

Earlier studies focusing on the Bi-modified Pt (111) surface attributed reversible Bi redox processes at peaks III/III' to a two-electron oxidation of metallic Bi to a $Bi(OH)_2$ or BiO species, depending on the solution pH [127, 128, 130 – 132]. The proposed oxidation state of Bi was solely based on charge evaluations from cyclic voltammetry. However, a recent XPS study [129] showed that Bi adatoms did not undergo any change in oxidation state. Based on XPS data in the oxygen range, voltammetric redox features in the range of peaks III/III' were associated with the coadsorption of an oxygen containing anion (OH^-). The proposed species is symbolised as ($Bi_{ad} \cdot OH^-$) representing some coadsorbed state of metallic Bi and hydroxide ions. Up to now, Bi redox processes and pH dependencies at higher overpotentials are still not quite clear. Thus, RRDE experiments provide some information on the processes involved. At pH = 0, processes II, I, and I' are clearly associated with the dissolution and deposition of Bi ions (Figure 4.8(a)). These ions most likely involve species like Bi^{3+}, $Bi(OH)_2^+$ or $Bi(OH)^{2+}$ [133]. On the cathodic scan, underpotential deposition of Bi extends to potentials of peak III' yielding a net deposition of Bi during CV. This has been observed previously [134] and explains the obvious asymmetry when comparing the measured cathodic and anodic ring charges in Figures 4.8(a) – 4.8(c).

4.3.2 Oscillatory formic acid oxidation on Pt modified by Bi deposition

Figure 4.9 illustrates the effect of Bi adatoms on the formic acid oxidation on a Pt electrode. Figure 4.9(a) shows the typical cyclic voltammetry profile (dotted line) on an pure Pt electrode, while an about five times higher electro-oxidation current of HCOOH on the Bi-modified Pt electrode is observed (solid line). According to previous studies [128, 134, 136], this higher electrocatalytic activity of Bi/Pt for HCOOH oxidation can be due to two modification effects of Bi adatoms such as a third-body effect on a Pt (100) and an electronic effect on a Pt (111). In this work, polycrystalline Pt was used, and thus one can speculate that the enhanced current may be the result of both steric hindrance of the formation of poisoning species (CO) and intrinsic kinetic enhancement [87, 137, 138]. The value of the oscillatory current related with formic acid oxidation is significantly higher than that on pure Pt. This oscillation is observed over a broad potential region between + 110 mV to + 280 mV and it indicates periodic activating and passivating processes of the electrode. This result is in good agreement with previous studies that the current for formic acid oxidation may increase by up to a factor of 50 [139]. The oscillatory cyclic voltammetry was found to be reproducible for many successive voltammetric cycles.

The potential parameter dependence of the current oscillations exhibits the following interesting features. Current oscillations with high frequency and small amplitude abruptly set in on the left flank of the peak on the anodic scan. At the onset of oscillations, a stationary current-potential curve with positive slope (Figure 4.9(a)-I) is obtained, while at higher anodic overpotential, an current-potential profile with negative slope (negative differential resistance) shows higher amplitude and smaller frequency oscillation (Figure 4.9(a)-II). Analysis of Figure 4.9 suggests that the formation of Bi surface oxides leads to a relatively rapid decline in the high currents between + 220 mV and + 280 mV. On the other hand, a very high coverage of metallic Bi (below – 200 mV) decreases the oxidation current, since Bi on the Pt electrode inhibits the adsorption of HCOOH. Interestingly, as sketched in Figure 4.9 (see inset), the average value ($<I_{osc}>$) of the oscillatory current during HCOOH oxidation on Bi/Pt electrode is higher than that of the (extrapolated) stationary operation points at the same applied potential. Accordingly, direct formic acid or methanol oxidation under autonomous

oscillatory conditions and/or by applying external pulses can lead to an increased power output.

A correlation of oscillatory voltammetry in Figure 4.9(a) and Bi redox features in Figure 4.7(b) in the solution without formic acid may offer valuable clues as to the chemical surface processes that occur under oscillatory conditions. However, a direct comparison of Figure 4.9(a) with CV profiles without formic acid on Bi-UPD Pt (Figure 4.7(b), dotted line) is not possible due to the uncompensated solution resistance. Thus, corrected for the ohmic potential drop ($IR_{solution}$) the curve plotted as solid line in Figure 4.10(b) refers to the true interfacial potential. In Figure 4.9(b) (1×10^{-6} M Bi^{3+}), one recognises the current step to occur near the cathodic onset of the second plateau (II), which marks the beginning of Bi oxidation on the surface (see Figure 4.8).

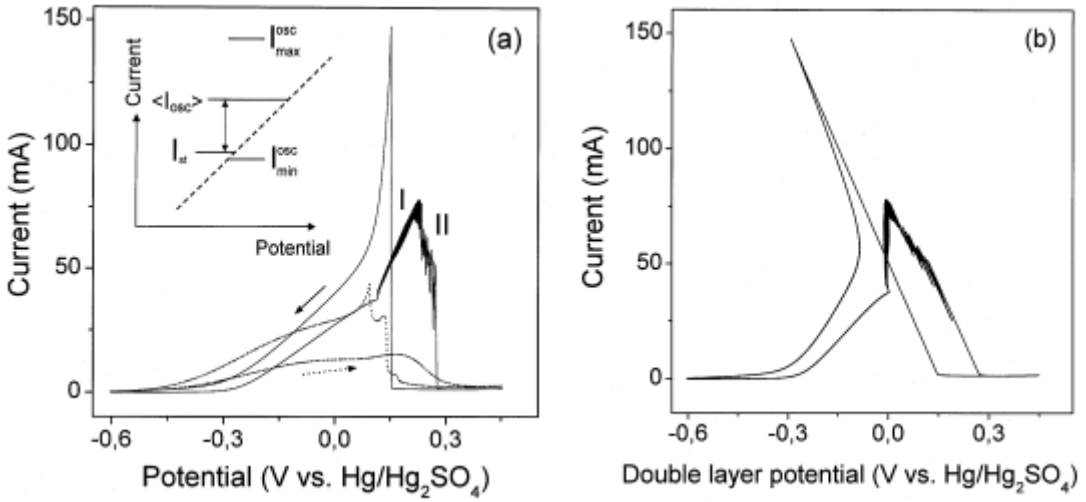

Figure 4.9. (a) Cyclic voltammetry of electro-oxidation of formic acid in the absence of Bi^{3+} (dotted line) and in the presence of Bi ions of 1×10^{-6} M (solid line). (b) IR correction of CV of Figure 4.9(a) in order to allow comparison with the potentials of Bi deposition/dissolution of Figures 4.7 and 4.8. Electrolyte is 0.1 M HCOONa/0.033 M H_2SO_4 and scan rate is 5 mV/s. The inset schematically shows that oscillatory systems can exhibit an advantage in the current yield. Extrapolation of the stationary current suggests that this may be the case in the present system.

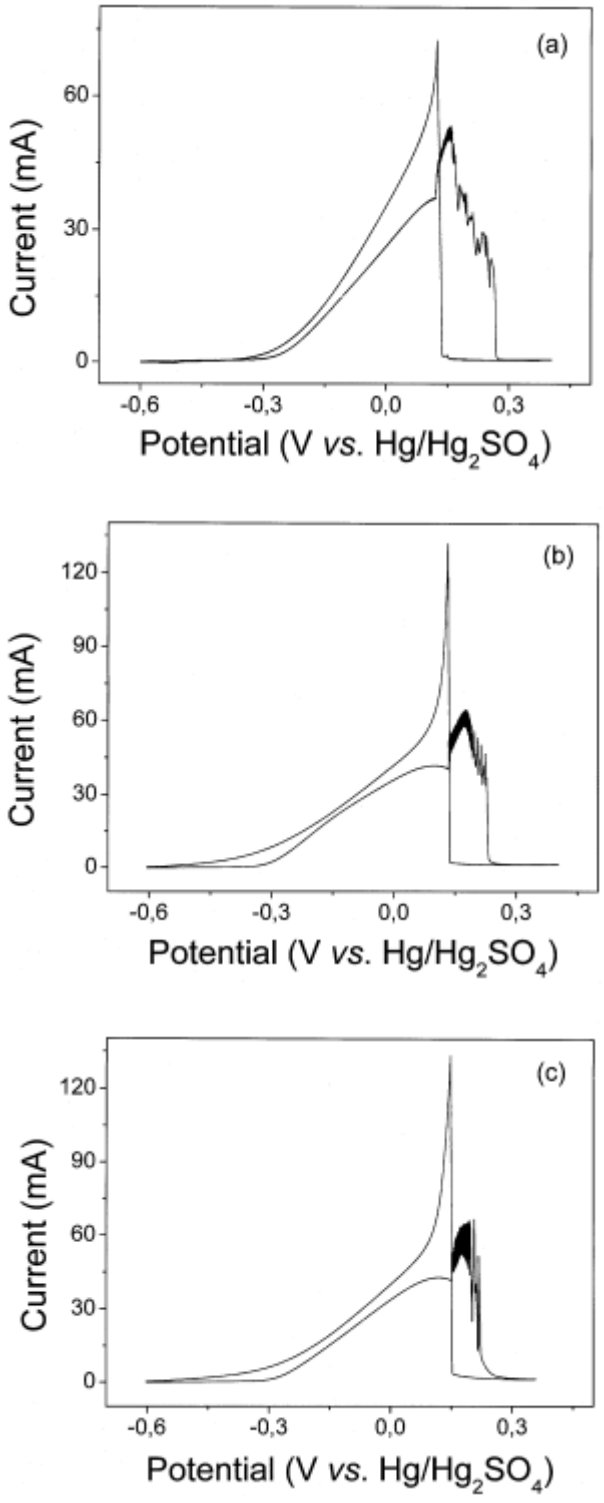

Figure. 4.10. Current-potential profiles of formic acid electro-oxidation in the presence of Bi–UPD. (a) 1×10^{-5} M Bi^{3+}, (b) 1×10^{-6} M Bi^{3+} and (c) 5×10^{-7} M Bi^{3+}. Bulk solution is 0.1 M HCOONa/0.033 M H_2SO_4. Scan rate is 10 mV/s.

For all three different concentrations of Bi ions investigated, the anodic current spikes indicate sustained current oscillations when the outer potential U is fixed. Increasing the Bi concentration results in a lower value of the abrupt onset potential of the oscillatory behaviour, and it also leads to a decrease in the stability and the reproducibility of the oscillatory operating states, cf. Figure 4.10(a) with 4.10(c). Cyclic voltammetry of the Pt ring modified by irreversible open circuit potential (OCP) deposition of Bi adatoms showed a higher current density compared with that on the pure Pt ring. But this CV did not exhibit current oscillations on the anodic scan. On the other hand, underpotential modification with Bi at -320 mV induced current oscillations on only the first and second anodic scan. Although the observed current during CVs is still significantly larger than on pure Pt, neither current spikes nor stationary oscillations are observed from the third anodic scan. When scanning during one of the first two CVs is stopped in the oscillatory region, the resulting current oscillations rapidly decline in amplitude and have significantly shorter lifetimes than that in the presence of Bi ions in the main solution. Subsequent cycling could not bring back oscillatory spikes. If a small amount of Bi ions (5×10^{-7} M Bi^{3+}), however, are now added to the bulk electrolyte, the original oscillatory phenomena of HCOOH on Bi–UPD/Pt return and have a longer lifetime of current oscillations than UPD modification.

Impedance spectroscopy

To analyse the mechanistic origin of the current oscillations in Figure 4.9, the electrochemical impedance spectra were measured prior to the onset of periodic oscillations. Nyquist plots at three different applied potentials U are shown in Figure 4.11. At the outer potential (U) of +70 mV (Figure 4.11(a)), the impedance plot $Z(\omega)$ exhibits a clockwise capacitive-inductive loop indicating dynamically stable stationary operating points. On the other hand, the impedance plot is drastically changed at +80 mV in Figure 4.11(b). $Z(\omega)$ wraps around the origin counter-clockwise, which means that we obtain the intersection between the real axis and $Z(\omega)$ where Z becomes real and negative at a finite frequency ω_0 of $5 \sim 6$ Hz. $Z(\omega)$ again exhibits positive real resistances for very low frequencies.

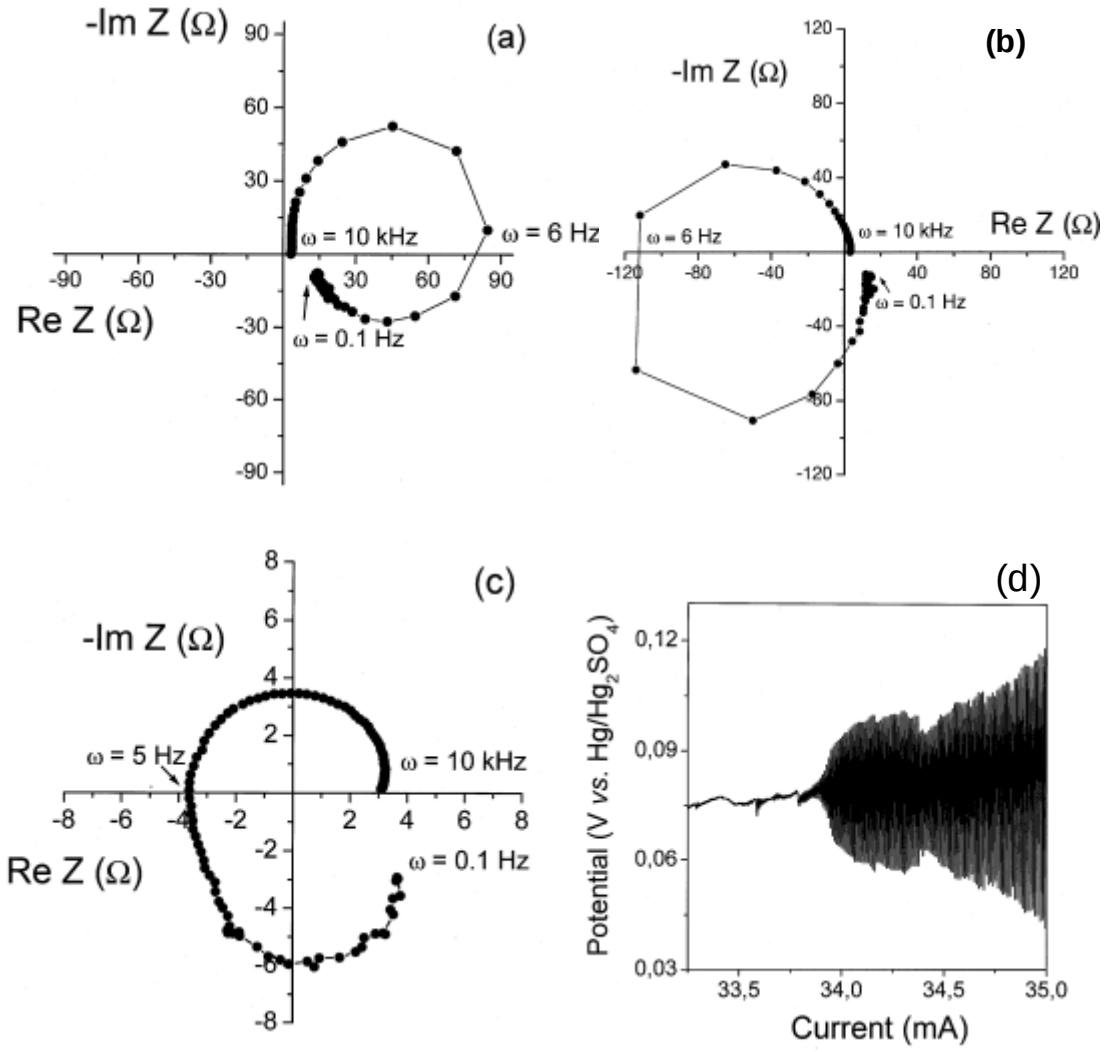

Figure 4.11. Electrochemical impedance data of the HCOOH oxidation on Bi-modified Pt: (a) + 70 mV, (b) + 80 mV, (c) + 130mV and (d) onset of sustained potential oscillations (Hopf bifurcation) in the galvanostatic mode with a scan rate of 0.05 mA/s in 0.1 M HCOONa/0.033 M H_2SO_4 with 1×10^{-6} M Bi^{3+}.

The detailed shape of the Nyquist plot bears information on the mechanistic origin of the oscillatory behaviour, which can be used to predict the dynamical stability of oscillatory systems. The significance of the distinct value ω_0 in Figures 4.11(b) and 4.11(c) where Im Z = 0 with Re Z < 0 becomes clear in galvanostatic oscillations (see Figure 4.11(d)). A galvanostatic scan of the formic acid oxidation results in an onset potential of sustained oscillations between + 70 mV and + 80 mV with an initial oscillation frequency of *ca.* 5 Hz. As discussed in previous work [30, 140, 141], the

critical potential, where the Nyquist plot crosses the negative real axis, marks the galvanostatic transition to periodic behaviour, *i.e.*, Hopf bifurcation. The value of ω_0 represents the intrinsic frequency of oscillation in the electrocatalytic oxidation of HCOOH on Bi/Pt.

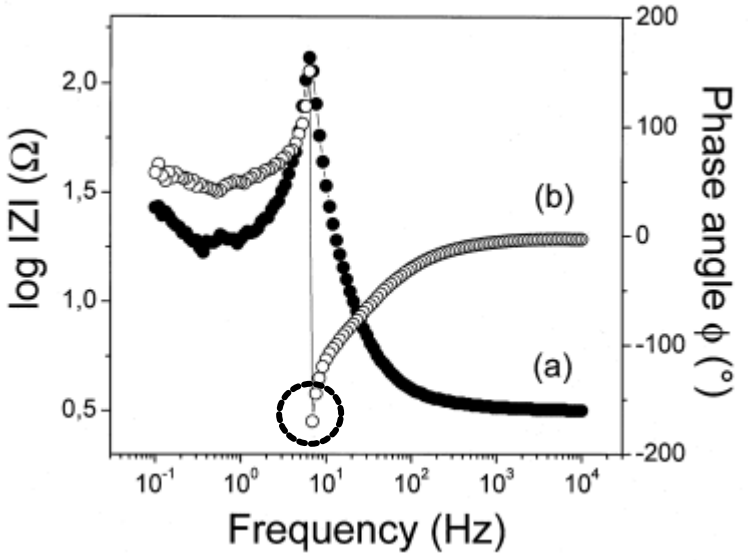

Figure 4.12. Bode plot at + 80 mV clearly demonstrates that the phase angle jumps from –180 ° to +180 ° (dotted circle) at frequency ω_0 = *ca.* 5 Hz, *i.e.*, this drastic phase change results in an anti-clockwise impedance profile in the Nyquist plot (Figures 4.11(b) and 4.11(c)).

Figure 4.12 is the Bode plot at outer potential of + 80 mV, which clearly shows that the drastic change of phase angle from –180 ° to +180 ° (see dotted circle) at frequency ω_0 = *ca.* 6 Hz results in an anti-clockwise impedance profile in the Nyquist plot (Figures 4.11(b) and 4.11(c)).

Mechanistic discussion

In the formic acid oxidation on pure Pt, poisoning by adsorbed CO was shown to play an important role in the oscillation mechanism [57, 63]. Adsorbed CO is removed reactively as soon as OH adsorption sets in. In the presence of Bi, less CO forms and is removed presumably by reaction with Bi oxygen species. Thus, although some CO may still be formed on Bi-modified Pt, the oscillation mechanism can be rationalised even if

we neglect CO, as follows. First of all, note that under the conditions in question most of the Bi is irreversibly adsorbed, which causes a significant increase in current (compared with pure Pt). In contrast, additional amounts of Bi (which reversibly deposit and redissolve) cause the current to slightly decrease again. Increasing amounts of oxygen species (most likely Bi oxides) form between 0 and + 0.2 V (cf. Figures 4.8(c) and 4.9(b)), which cause a significant current decrease. Starting at a high current state during the oscillatory cycle near the onset, the potential ϕ is relatively low, namely between peaks III and II (cf. Figures 4.8 and 4.9(b)). Here the Bi adlayer is expected to exist as a metallic state [130]. Due to potential controlled Bi deposition, the Bi coverage reaches values above the limit reached by irreversible open circuit potential (OCP) deposition. The resulting Bi adlayer becomes denser [131] and causes a drop in electrocatalytic oxidation current I of HCOOH. According to the following relation, U = IR + ϕ, the interfacial potential ϕ now gradually rises, until at the onset of peak II, ϕ reaches a point where the reduced Bi adatoms undergo a stepwise transformation to Bi (III) oxides. In a first step, the metallic Bi_{ad} is oxidised to insoluble BiO_{ad} as follows,

$$Bi_{ad} \cdot OH^- \rightarrow BiO_{ad} + 2e^- + H^+. \qquad (4.1)$$

The presence of adsorbed BiO on the Pt surface decreases its catalytic activity. Therefore, ϕ increases, yielding a self-enhancing feedback loop towards higher potentials ϕ and the deactivated BiO state. In a second step, BiO_{ad} is oxidised to a Bi (III) species, which is still adsorbed on the surface,

$$BiO_{ad} \rightarrow BiO_{ad}^+ + e^-. \qquad (4.2)$$

Then the adsorbed BiO^+ dissolves,

$$BiO_{ad}^+ \rightarrow (BiO_{sol}^+)\uparrow. \qquad (4.3)$$

Therefore, the effective coverage of Bi oxide is reduced down to the lower limit value of irreversibly adsorbed Bi. The oxidation current increases on the slow time scale of Bi (III) dissolution, which stops the positive feedback in ϕ. With increasing current

(I), ϕ starts to decrease again. At more cathodic potentials, the residual Bi oxide is reduced and additional deposition of Bi sets in until the Bi adlayers reach their initial metallic state, $Bi_{ad} \cdot OH^-$. If one assumes that the initial oxidation step to BiO is sufficiently fast, one can expect negative impedance on this fast time scale, while positive impedance follows on a time scale of the slow Bi (III) dissolution. This is confirmed by the measured impedance curves given in Figure 4.11 and Figure 4.12 showing a hidden negative differential resistance (HNDR) with a non-zero frequency. As in previous work on electrochemical oscillators [30, 140], the formic acid oscillator on Bi/Pt can be categorised into the mechanistic class IV of HNDR oscillators, most likely into the IV.2 subclass [140]. The above mechanistic hypothesis resembles the processes of the oscillatory H_2 oxidation on Pt in the presence of anions and electrosorbing cations [142, 143], *i.e.*, it consists of a slow process with positive and a faster with negative impedance. Further away from the onset, oscillations persist on a branch in the CV with negative differential resistance (NDR). While the irreversibly adsorbed Bi remains on the surface in this region, no additional deposition/redissolution takes place any more (cf. Figure 4.8). Consequently, the mechanism is expected to be of NDR type (class III according to Ref. [141]). The negative differential resistance is caused by increasing poisoning by adsorbed oxygen with increasing potential, the slow negative feedback loop is most likely due to the transport of formic acid to the electrode (cf. [57, 63]).

Effect of external resistance R_{ex}

Analysing the electrochemical impedance spectroscopy measurements (see Figure 4.11), a solution resistance of 3Ω was obtained, in good agreement with the calculated value of the solution resistance. In order to prove this value, we have investigated the CV by applying various external resistances (R_{ex}) during oscillatory HCOOH oxidation on the Bi-modified Pt electrode. Figure 4.13 shows that with increasing R_{ex}, the onset of the current oscillation on the anodic scan occurs at a higher anodic overpotential. Comparing Figure 4.9(a) (solid line) with 4.13(a) at $R_{ex} = 2\,\Omega$, one can clearly observe that the response of oscillatory current becomes synchronised, while the application of a higher R_{ex} of 5 Ω (see Figure 4.13(b)) tends to decrease the reaction current due to increasing ohmic resistance. In Figure 4.13(c), the onset

potential of the current oscillations is obtained at a much higher outer potential of + 315 mV than that without applying external resistance. However, after IR correction where R is sum of R_s and R_{ex} (R = 10 Ω in this case), the initiation of current oscillations as shown in Figure 4.13(d) occurs around a double layer potential of – 50 mV, and it is similar to the double layer potential observed in Figure 4.9(b). Additionally, the bistable region on both scans increases with increasing external resistance and it resembles the data which result from a larger distance between working ring electrode and reference electrode, *i.e.*, a larger uncompensated resistance (R_u).

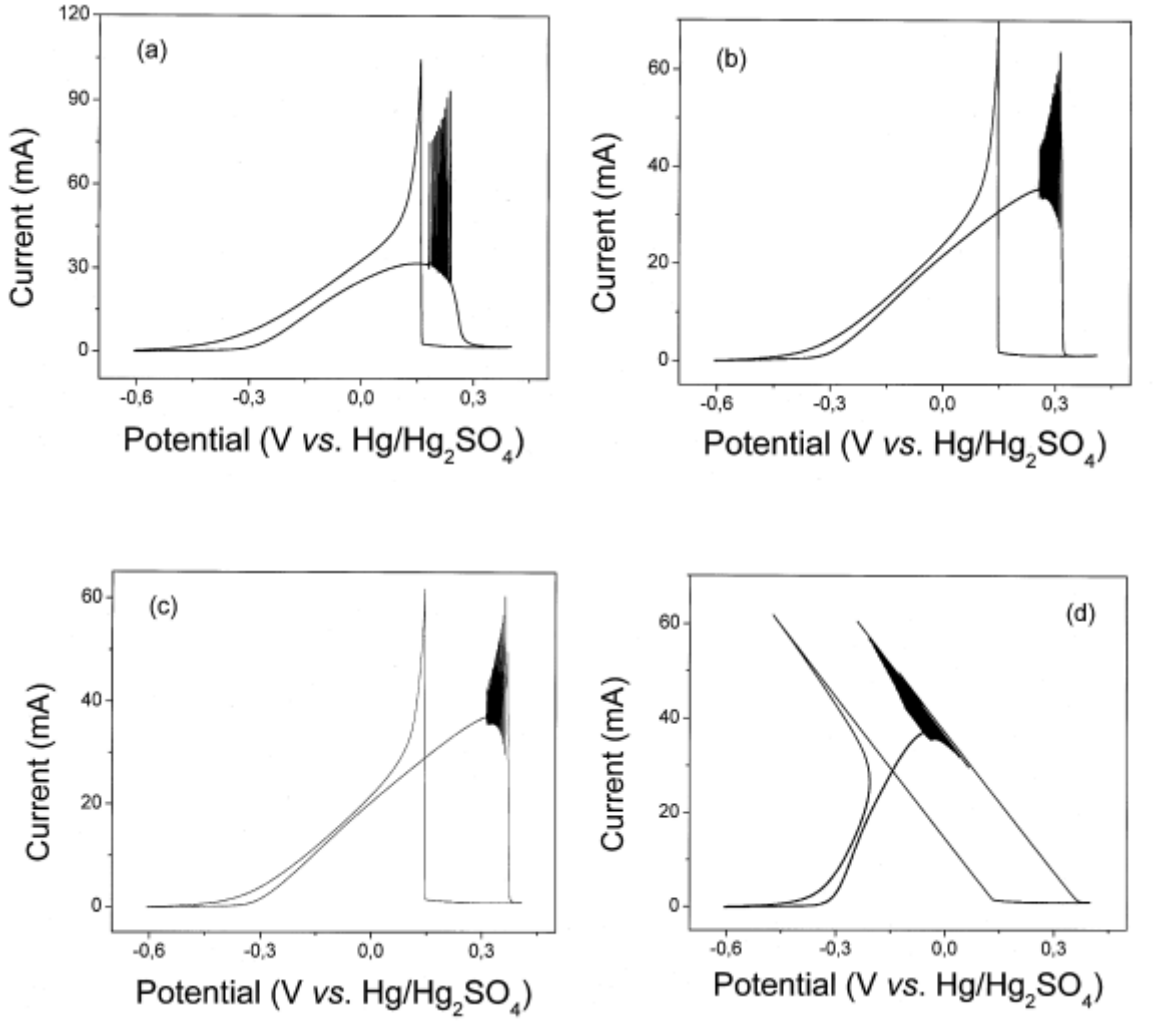

Figure 4.13. Cyclic voltammetry of electrocatalytic oxidation of formic acid on Bi/Pt electrode applying different external resistance. (a) 2 Ω, (b) 5 Ω, (c) 7 Ω and (d) the plots were obtained after correction for ohmic potential drops across the electrolyte as determined from impedance measurements at large frequencies (R_{ex} = 7 Ω).

4.4 Spatiotemporal interfacial potential pattern formation during the electro-oxidation of HCOOH on Bi/Pt

In this section, experimental observations of the spatiotemporal dynamics in the electrocatalytic oxidation of HCOOH on the Bi-modified Pt ring electrode are reported. Bi modification significantly enhanced the current density and was found to considerably increase the existence range of oscillations and spatiotemporal self-organisation. Reversible pattern transitions between travelling pulses and oscillating standing waves were observed when the outer potential or the concentration of HCOOH near the electrode was used as control parameters. Experimental results were compared with computer simulations of a reaction-migration system. Finally, the role of electrode inhomogeneities in pattern formation and the transitions between patterns are discussed.

4.4.1 Spatial patterns in the interfacial potential

This section deals with the spatiotemporal distribution of the local electrode potential underlying the oscillatory instability. Due to negligible solution resistance between potential microprobe and WE, the local potential essentially reflects the interfacial electrode potential. To monitor the instantaneous local interfacial potentials on the Pt ring WE, 11 (or 12) potential microprobes were equi-spaced (in 30° angle) along the WE (see Figure 4.1). Each microprobe consisted of a glass tube with a microcapillary (inner diameter: *ca.* 200 µm) at one end. The microprobes capped with a commercial Hg/Hg_2SO_4 electrode were filled with a 0.5 M Na_2SO_4 solution (Merck, p.a.) and mounted one by one into the Teflon lid, followed by careful alignment of all capillary tips with respect to the Pt ring WE. The distance between WE and the end of the capillary of the microprobes was 0.2 mm. The spatial positions along the WE as reported in the following experimental data are numbered from 1 to 11 (or 12) and directly correspond to the respective position of one of the potential probes. All local probe potentials reported hereafter refer to the instantaneous potential difference between the WE and the opening of the tip of the respective microprobe. Neglecting the

remaining ohmic potential drop, the probe signals represent a good approximation to the instantaneous local interfacial potentials of the WE. The probe signals were sampled at 1 kHz with their noise level being less than 1 %.

Figures 4.14(a) and 4.14(b) show the cyclic voltammetry and corresponding spatial change of the interfacial potential in 0.5 M H_2SO_4 (without adding formic acid solution) on the Bi-modified Pt ring electrode. This control experiment shows that the potential response of all microelectrodes is homogeneous, *i.e.*, there is no distinct spatiotemporal pattern of the interfacial potential due to any defect of the microprobes.

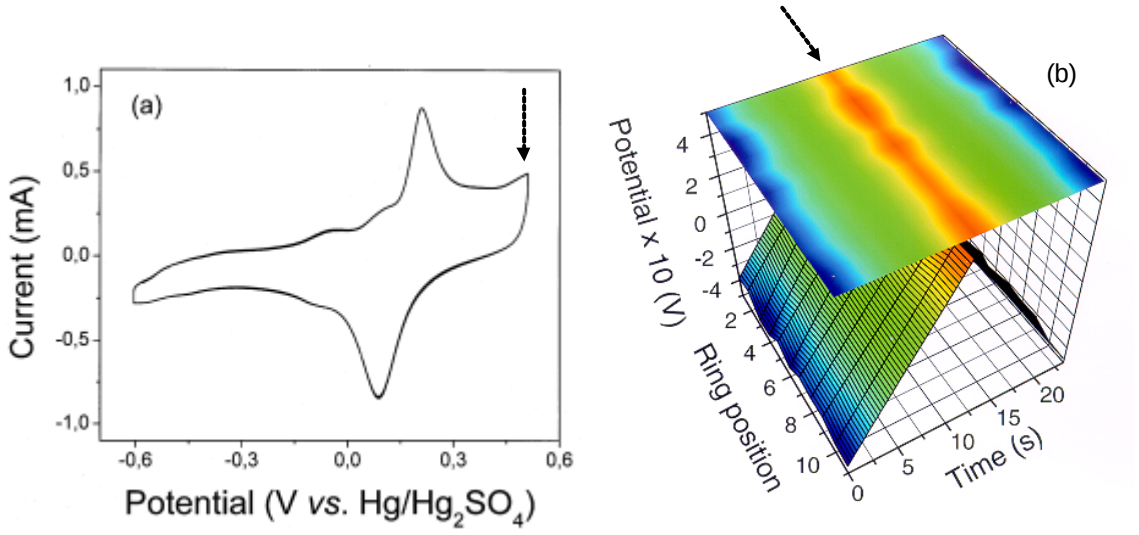

Figure 4.14. Cyclic voltammetry in 0.5 M H_2SO_4 with 1×10^{-5} M Bi^{3+} on a Pt working electrode with scan rate of 50 mV/s. (a) Temporal data and (b) (colour) spatiotemporal behaviour of interfacial potential. Dotted arrow indicates the scan reverse.

In order to better understand the poisoning and reactivating behaviour at the electrode (which need by no means occur homogeneously), the spatiotemporal evolution of the interfacial potential was recorded. The reference electrode (in the centre of the ring) is close to the WE, which causes the migration coupling to become negative with increasing distance [14, 21], such that opposite areas on the ring tend to be anti-correlated.

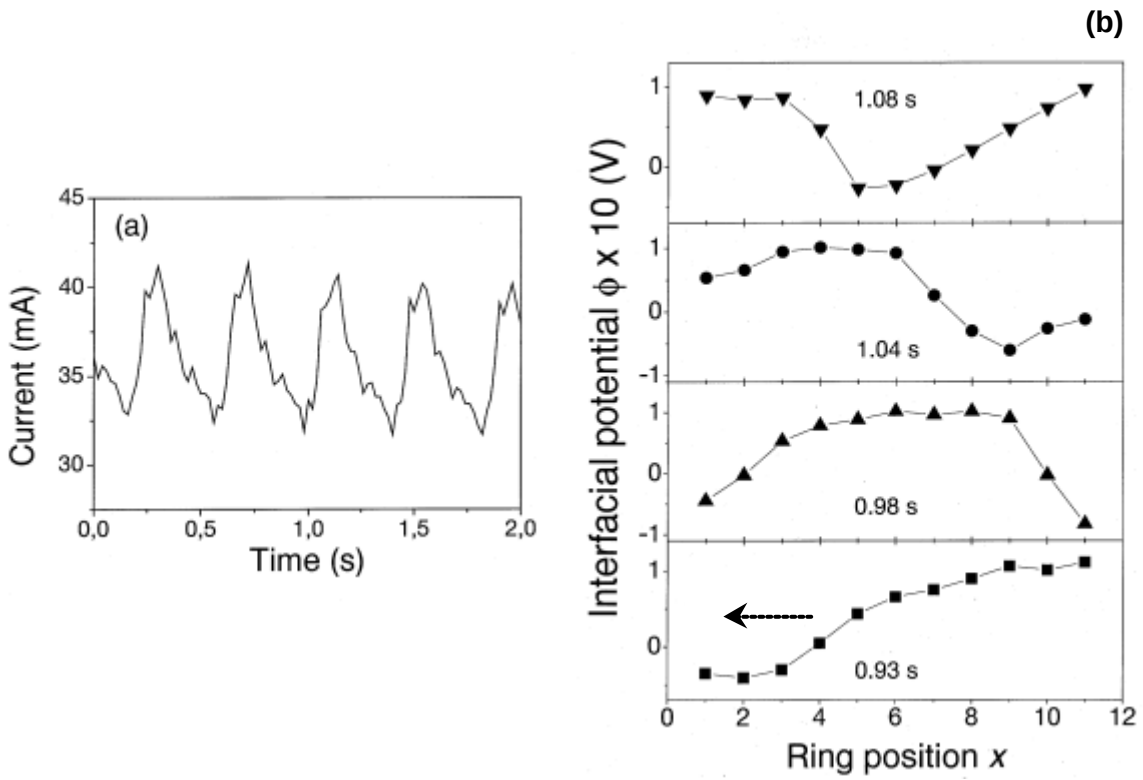

Figure 4.15. (a) Current profile at constant outer potential (U) of + 150 mV and (b) temporal sequence of instantaneous spatial travelling pulse at Pt ring position of 6. The time interval between two successive profiles is 40 – 50 ms.

The temporal current response and a two-dimensional space-time plot of the local potential along the Pt ring electrode are shown in Figure 4.15 when constant outer potential (U) is applied. According to $U = IR + \phi$, a higher interfacial potential (ϕ) corresponds to low local catalytic activity due to poisoning, while low values of the interfacial potential make a large contribution to the total current (active). Figure 4.15(a) represents sustained current oscillations. Figure 4.15(b) exhibits a temporal sequence of the distribution of the interfacial potential on the ring electrode and it clearly shows the travelling character of a passivating domain pulse. Note that the travelling pulse changes its size and shape periodically (due to imperfection of the electrode) which gives rise to oscillations in the total current.

4.4.2 Pattern sequences on the cyclic voltammetry

Figure 4.16(a) shows the temporal signal of current oscillations during a cyclic voltammetry (CV) with a scan rate of 5 mV/s. The behaviour in the time domain reveals a transition from harmonic large-amplitude oscillations to a complex pattern of smaller peaks. The spatial patterns underlying the anodic scan of Figure 4.16(a) are reported in Figures 4.16(b) – 4.16(d). At the beginning of the oscillations, the potential distribution in Figure 4.16(b) clearly represents standing waves (*SW*), while travelling pulses prevail at higher overpotentials (Figure 4.16(d)).

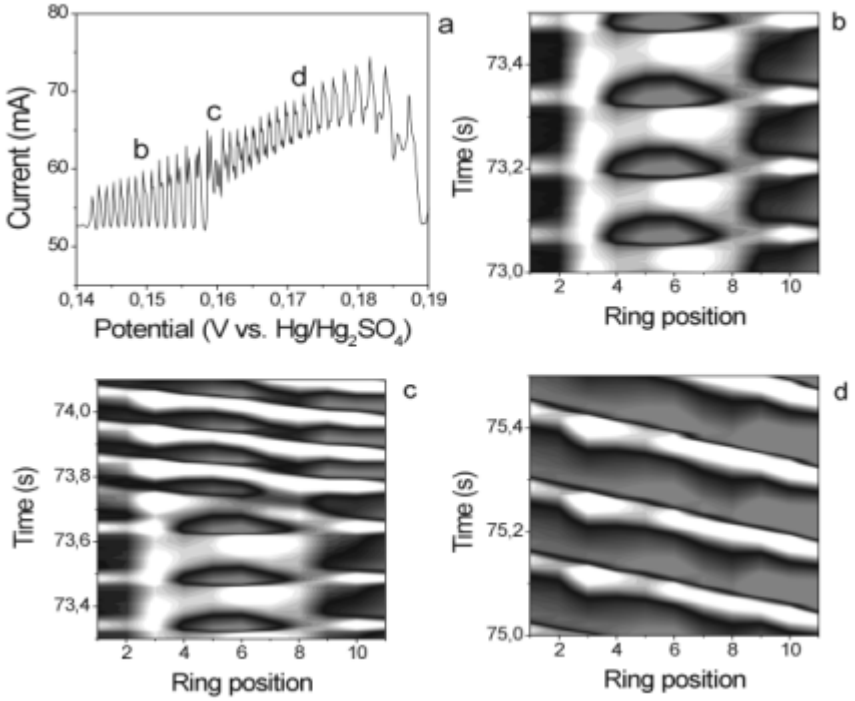

Figure 4.16. (a) Oscillatory current-potential profile during slow anodic scanning. The change in the waveform near t = 74.5 s indicates changes in the spatial dynamics. Figures 4.16(b) – 4.16(d). Spatiotemporal profiles of the interfacial potential corresponding to Figure 4.16(a). Figure 4.16(b): oscillatory standing wave (SW) regime, Figure 4.16(c): pattern transformation from *SW* to *Pulse* and Figure 4.16(d): travelling pulses. Scan rate is 5 mV/s and the electrolyte is 0.1 M HCOONa/0.033 M H_2SO_4 with 5×10^{-7} M Bi^{3+}.

When reversing the anodic scan within a pulse regime, the pulse velocity first became more and more inhomogeneous along the ring. Then, the spatiotemporal dynamics passed through the transition state, before it came back to *SW*. Oscillatory

standing waves (*SW*) were recently described in the electrocatalytic oxidation of formic acid on unmodified Pt electrodes [22]. It is characterised by the sustained periodic alternation of an active (high interfacial potentials) and a passive (low interfacial potentials) domain in space-time without spatial propagation. However, these standing waves do not seem to arise from the same bifurcation as in Figure 4.16; most likely, they are caused by propagation failure of pulses due to surface inhomogeneities.

4.4.3 Pattern sequences at fixed applied potentials

Figure 4.17(a) depicts the time-periodic evolution of the total current when keeping the applied potential U in the middle of the oscillatory range on the anodic scan. First, the time average of the integral current slowly decreases exhibiting a complex oscillatory regime of relatively small amplitude. Then, after some time, the shape of the oscillations suddenly undergoes a distinctive transformation to a period−2 regime with larger amplitude. Figures 4.17(b) – 4.17(d) show the corresponding processes in the local electrode potentials. The initial dynamics represent travelling catalytic pulses, as shown in Figure 4.17(b). At the transition the pulse stops, giving way to a dynamic regime of oscillatory standing waves (Figure 4.17(c)), which subsequently remain stable for long observation times (Figure 4.17(d)).

Without forced mass-transport, high-amplitude current oscillations at fixed U observed in Figure 4.17 usually entail gradual depletion of dynamical volume species such as the local concentration of an electroactive species at the electrode. But driven into the mass-transport limited regime, the dynamics of the system may be significantly altered. In order to investigate effects of mass-transport on the pattern forming processes, N_2 bubbling (forced convection) was applied, as shown in Figure 4.18. Reproducible pattern formations, standing waves (*SW*), travelling pulse (*Pulse*) and defect-mediated standing waves (*DSW*), are sequentially observed by repetitive restoring of the original mass-transport conditions, *i.e.*, repeated replenishment of the species near the surface through forced convection. Obviously, the important parameter for the observation of the spatiotemporal patterns is the local concentration drift of the species near the electrode.

Theoretical simulation at different concentrations of HCOOH (Figure 4.19) confirms experimental pattern sequences derived by depletion of active species.

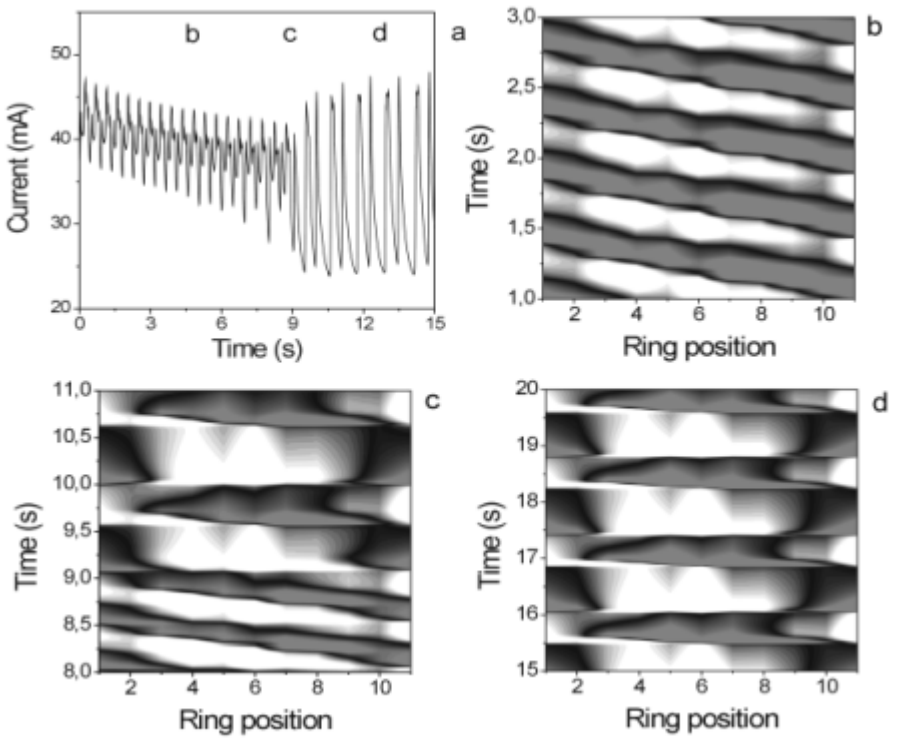

Figure 4.17. (a) Sustained current oscillations at constant applied potential U. A qualitative change in the oscillatory waveform (around t = 9 s) indicates changes in the spatial potential distribution. Figures 4.17(b) – 4.17(d) Spatiotemporal profile of the interfacial potential corresponding to the time series (b – d) in Figure 4.17(a). (b) Travelling catalytic pulses, (c) propagation failure of pulses and (d) final oscillatory standing wave regime most likely due to defects blocking the transition of pulses. Experimental conditions: constant U is + 152 mV and the electrolyte is 0.1 M HCOONa/0.033 M H_2SO_4 with 1×10^{-6} M Bi^{3+}.

Spatiotemporal pattern in galvanostatic scans

Figure 4.20 shows the spatiotemporal pattern of the interfacial potential during galvanostatic potential oscillations. One can clearly see that there is in-phase spatiotemporal oscillation. It is due to the positive migration coupling along the working electrode [27]. Synchronised potential oscillations can be also obtained in the presence of an external resistance and/or when the reference electrode is sufficiently far away from WE to induce global coupling.

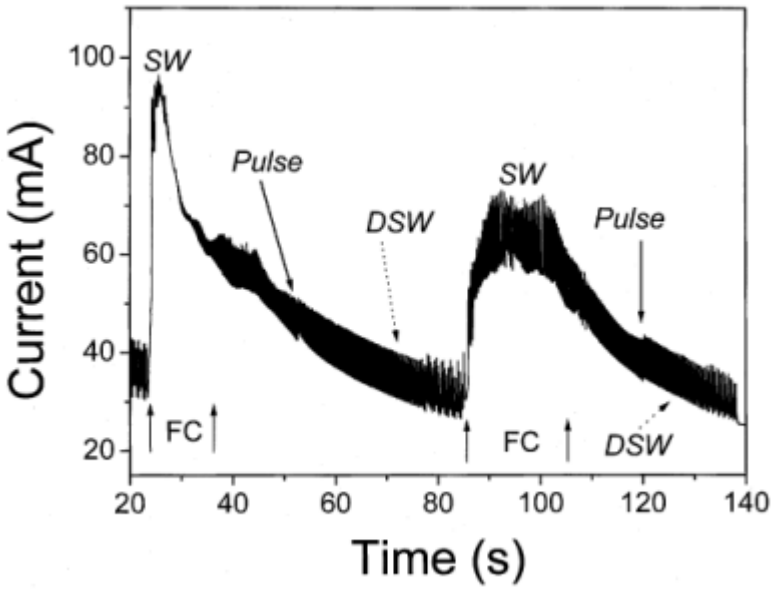

Figure 4.18. Effect of forced convection on the current oscillations and the corresponding potential patterns at constant outer potential. Experimental conditions as in Figure 4.17 (forced convection: FC, standing waves: *SW*, travelling pulse: *Pulse*, defect-mediated standing waves: *DSW*).

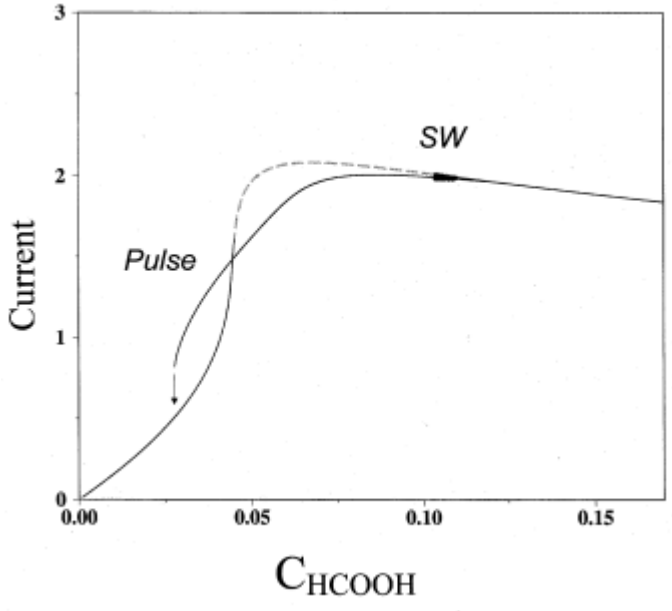

Figure 4.19. Theoretical simulation of a pattern formation sequence as a function of the concentration of HCOOH at constant outer potential (standing waves: *SW*, travelling pulse: *Pulse*). Courtesy of J. Christoph [27].

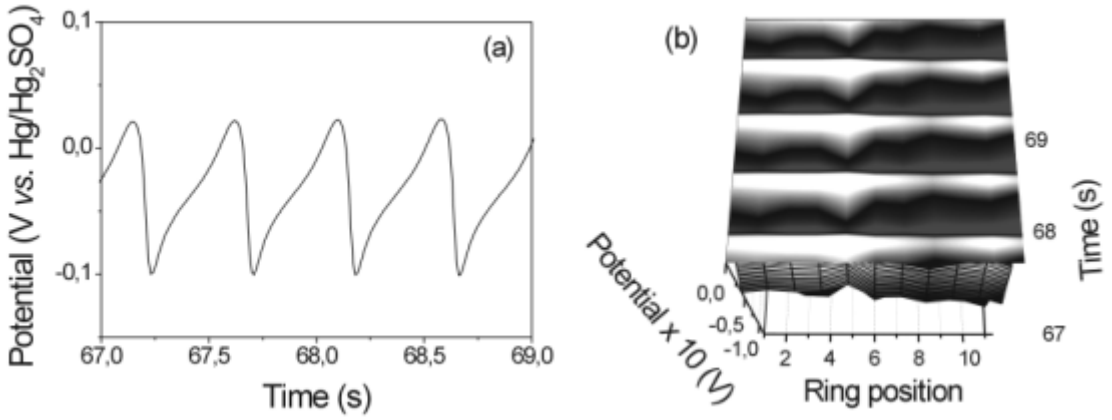

Figure 4.20. (a) Sustained potential oscillations with increasing current and (b) spatiotemporal profile of the interfacial potential representing in-phase oscillations. Experimental conditions: scan rate is 50 μA/s, 0.1 M HCOONa/0.033 M H_2SO_4 with added 1×10^{-6} M Bi^{3+}.

4.4.4 Autonomous pulse reversal on a ring surface

To fully understand the organising mechanisms of the transitions between distinct potential patterns (bifurcation), aside from controllable parameters (system constraints) such as bulk concentrations or applied potential, the organising role of surface points with slightly varying catalytic properties (surface defects) has to be considered. While changes in constraints are sufficient to organise bifurcation when one pattern becomes unstable in favour of another, defects continuously act as perturbations and may mediate between two coexisting stable dynamical states when their perturbing effect becomes sufficiently strong. Hence, an experimentally observed bifurcation can be due to the combined effect of changes in control parameters and the action of defects. Figure 4.21 shows a space-time plot of a travelling pulse associated with oscillatory currents at fixed potential U. Approaching the ring positions $2-4$ at time $t = 234 - 235$ s, the pulse spontaneously stops short near ring positions $3-4$, followed by a reversal of its direction. Subsequently, the pulse reversal repeats close to the same locations when approached from the opposite direction.

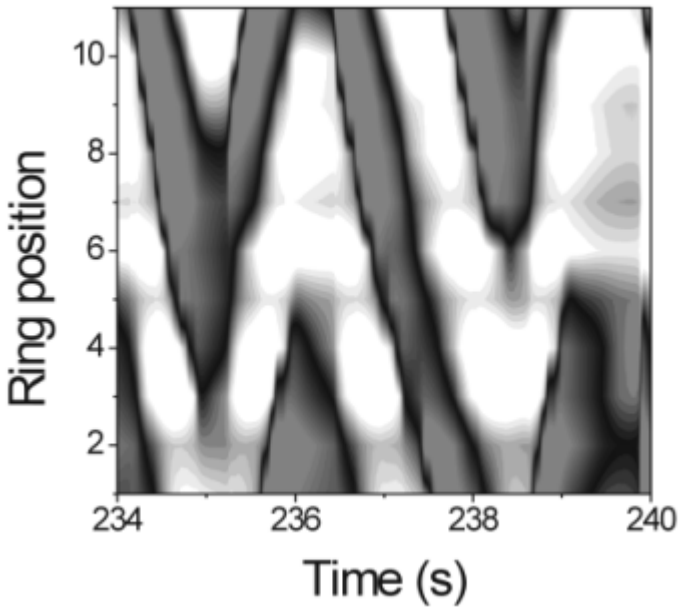

Figure 4.21. Defect-mediated reversal of direction of travelling catalytic pulses at fixed outer potential. Scan rate is 10 mV/s and the electrolyte is 0.1 M HCOONa/0.033 M H_2SO_4 with 5×10^{-7} M Bi^{3+}.

Obviously, electrode positions at 2 – 4 are more difficult to activate by a passing activation pulse and, therefore, may constitute a barrier for pulses with sufficiently low amplitude. If this occurs, the dynamic response of the system to the perturbation by the defect is the spontaneous transition to the (ideally equally stable) coexisting travelling pulse in the opposite direction. A detailed discussion of surface defects follows in Chapter 4.7 [24].

4.4.5 Discussion

Impedance spectroscopy showed that formic acid oxidation in the presence of Bi^{3+} is still an HNDR oscillator (hidden negative differential resistance). The negative resistance is (as in the absence of Bi^{3+}) due to site blocking by OH adsorption [57]. Adsorbed Bi largely suppresses the formation of CO on the electrode, which explains the significantly higher currents. The positive impedance on a slower time scale may nevertheless still be due to (some) CO formation, but here increasing Bi coverage at low overpotentials may also have a site-blocking effect.

The electrocatalysed oxidation of formic acid on Pt modified by Bi spontaneously undergoes transitions between different dynamic states, from homogeneous catalytic activity to states characterised by a spatiotemporally inhomogeneous distributions of the interfacial electrode potential (dynamical electrocatalytic potential patterns). The prevailing space-time patterns observed under the used ring electrode geometry have been oscillatory standing waves [22, 23, 144] as well as travelling electrocatalytic pulses [23], both associated with sustained oscillations in the total current. The patterns and the oscillations strongly depend on external control parameters such as the concentration of the solution and the applied potential.

Inhomogeneous distributions of the local potential at the electrified interface occurred around the maximum of the oxidation rate. Figure 4.22 experimentally demonstrates, for the first time, travelling activation pulses in an electrocatalytic reaction. In electrochemistry, travelling pulses were so far reported only during metal dissolution of Ni [12, 13] and Co in acidic media [14,17]. Aside from electrochemistry, travelling pulse dynamics can also occur in heterogeneous gas-phase catalysis under both isothermal [145] and thermokinetic conditions [146].

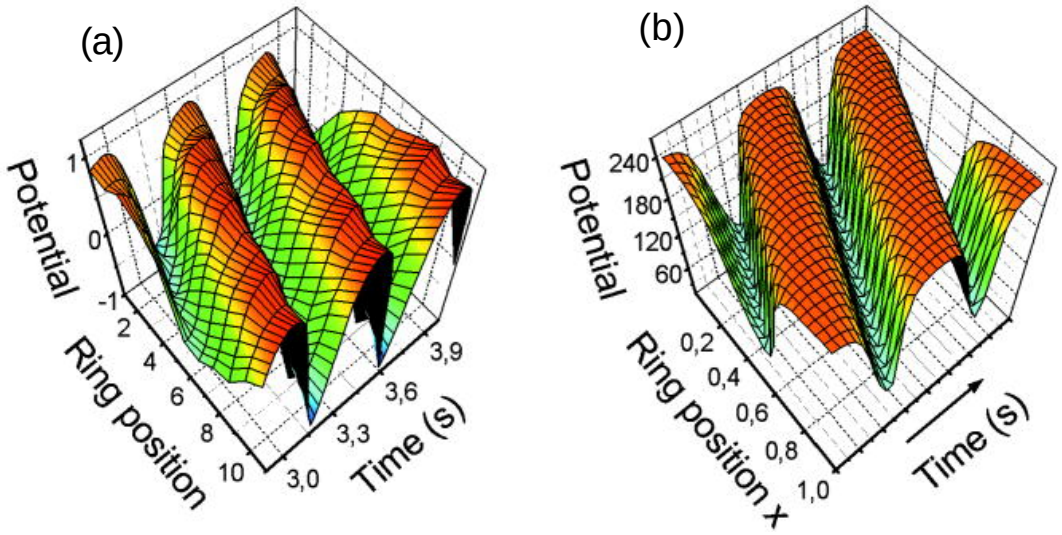

Figure 4.22. (Colour) Spatiotemporal distribution of the local interfacial potential during current oscillations at constant outer potential U (travelling catalytic pulse). (a) Experimental measurement (U is +150 mV and bulk conditions: 0.1 M HCOONa/0.033 M H_2SO_4 with 1×10^{-5} M Bi^{3+}) and (b) theoretical simulation of travelling pulse (for model details see Refs. [14, 27]).

An activation pulse is a travelling domain of high catalytic activity invading a passive region of the electrode. Thus, for periodic boundary conditions (ring electrode), each location on the WE becomes repeatedly reignited, and thus a stationary homogeneous deactivation of the entire catalytic interface is prevented. Ideally, pulses with a fixed domain size should yield a constant integral current signal for homogeneous system parameters. As shown in Figures 4.16, 4.17 and 4.22, however, surface inhomogeneities may constantly deform the pulse along the ring, resulting in an oscillatory integral current signal. The second interfacial potential patterns prevailing under the parameter chosen is oscillatory standing waves. These regimes involve spatially and temporally alternating domains of higher and lower activities with two fixed points of the electrode (nodes) of constant catalytic activity. Unlike metal dissolution reactions [147], standing waves were found to be the only ordered patterns in the electrocatalysed oxidation of formic acid on pure Pt electrodes [22]. The observed correlation between space-time dynamics and external system parameters such as concentrations and outer potential of U suggests a convenient strategy to control interfacial potential distributions in the electrocatalytic process in question.

Recently, a reaction-migration formalism introduced by Christoph [14, 27] presented a realistic theoretical and numerical description of pattern formation in electrochemistry. The distinctive approach of the model allowed the theoretical prediction of inhomogeneous patterns even with a complicated electrode geometry. Assuming the validity of the Laplace equation within the electrolyte, potential theory leads to an integro-differential equation for the description of the evolution of the interfacial (double layer) potential ϕ across the working electrode [14, 22]. The equation for ϕ consisted of (i) local faradaic reaction terms describing the detailed chemistry of the reaction, (ii) the local migration currents and (iii) an integral term accounting for the spatial migration coupling parallel to the electrified interface. The integral involved a spatial coupling function, H indicating the sign and strength of the coupling between two different points on the electrode. The qualitative shape of H was found to be critically dependent on the geometry of RE and WE. For the electrode geometry chosen, a ring type electrode H revealed a negative coupling of the interfacial potential between opposite points of the ring (negative long-range coupling), while adjacent points were coupled positively (positive short-range coupling). Negative coupling generally leads to a desynchronisation of the interfacial potential and, therefore, generally increases the

tendency of an electrochemical system towards the formation of inhomogeneous interfacial patterns. The mechanism used was a generic HNDR oscillator, including 2 chemical species, one of which adsorbs at lower and desorbs at higher potential (giving rise to a positive differential resistance), the other adsorbs (desorbs) at higher (lower) potential (causing a negative differential resistance). The latter is due to site blocking by OH adsorption in the present experimental system, while the former most likely corresponds to adsorbed Bi and/or CO.

Figure 4.23 shows the theoretical model predictions concerning the patterns in the interfacial potentials in dependence of the fixed applied outer potential. The bifurcation diagram was obtained for parameters and electrode geometry comparable to the present experiments, that is, under conditions of negative long-range coupling. For an illustrative explanation of the various regimes, a mode picture will be invoked. With increasing potential, the homogeneous active steady state (*hom. a.*) loses stability in favour of the first inhomogeneous mode consistent with the periodic boundary conditions of the ring. The space-time amplitude A of the resulting oscillatory standing waves (*SW*) is governed by a term like $A \approx a\,(t) \sin(2\pi / L \cdot x)$, where L and x are the circumference of the ring electrode and the spatial coordination along the ring, respectively. The function a (t) denotes the time-dependent amplitude of the standing wave. At higher values of the applied potential U, the amplitude a (t) of the active first mode strongly increases continuously exciting the corresponding, phase-shifted cosine mode by means of higher-mode coupling [27]. With one or more sine and cosine terms suitably superimposed, *SW* transform into pulse patterns at *ca.* + 420, which remain stable up to high values of U. Since either pulse direction is equistable in the model calculations, the resulting pulse direction is entirely determined by the initial conditions. Transitions between directions may only be achieved by perturbations (see Figure 4.21).

Finally, at high U, the system jumps to the homogeneous passive steady state. Reversing the potential scan, Figure 4.23 predicts the system to jump back to travelling pulses. In the simulations the pulse pattern remains stable up to the transition to the homogeneous active steady state. Generally, one-dimensional target patterns can coexist with travelling pulses near the homogeneous passive state (*hom. p.*), provided the difference in time scales of the variables is sufficiently large [27]. No target patterns are observed in the present experiments, but they have been reported previously in metal dissolution system [144].

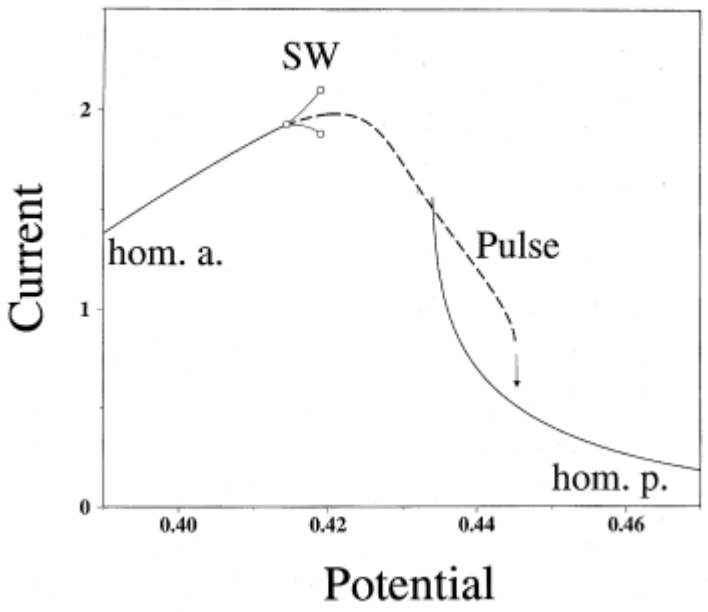

Figure 4.23. Numerical bifurcation diagram [23] illustrating stable spatiotemporal patterns of the double layer potential in dependence of the applied potential. For dynamic regimes that are associated with stationary integral migration currents (*hom.a., hom.p.* and *Pulses*), I is plotted *vs*. U. In the case of patterns standing wave patterns *SW*, which are associated with time-periodic currents, the current minimum and maximum are plotted on the y-axis (solid line: *hom. a.* = homogeneous active stationary state; *hom. p.* = homogeneous passive stationary state; open circles: *SW* = Standing Waves; dashed line: *Pulse* = Travelling Pulses). The diagram was calculated using a dimensionless HNDR model. Parameters were chosen such that the one-parameter diagram cut through the oscillatory regime.

While the predicted bifurcation sequences of Figure 4.23 on the anodic scan favourably compare with experimental results in Figure 4.16, the observed spontaneous transition from *Pulse* to *SW* on the negative-going scan seems to contradict the model. However, recall that Figure 4.23 represents the behaviour of an ideal reactive system with no spatial inhomogeneities in the parameters. In contrast, considering the measured pulse dynamics in Figure 4.16, the experimental electrode surface does exhibit points of varying catalytic activity (surface defects). If sufficiently strong, defects may mediate the transition between coexisting regimes, *e.g.*, in Figure 4.21 between regimes with opposite pulse direction. Scanning in the negative direction within the pulse regime, the amplitudes of the individual superimposed modes slowly decrease. At some critical

point, surface defects may be sufficient to suppress one (or more) of the inhomogeneous modes, for instance, if a passive defect happens to be near a point of high amplitude. In the simplest case of a travelling pulse made up by one sine and cosine mode, suppressing either of them leads to a reappearance of *SW*.

A similar line of argument can be invoked for the transition from *Pulse* to *DSW* in Figures 4.17 and 4.18. In the course of current oscillations at fixed applied potential, the average solution concentration of formic acid near the electrode surface, $c_{FA,}$ gradually decreases with time. This amounts to a constant drift in a control parameter driving the system slowly towards the stationary passive regime. Near the transition, the amplitude of the pulse decreases, making it more susceptible to the influence of surface defects. Finally, defects will give rise to non-rotating patterns, which may appear very similar to the initial standing waves, but are of different physical origin and do not arise from the same bifurcation scenario.

4.5 Phase resetting and controlled pulse reversal on a ring electrode

In an excitable medium the excitation is usually confined to a small region of space propagating with a certain velocity. The return to the initial state of the element of an excitable medium and a diffusional flow to a neighbouring element of the medium result in the propagation of a travelling pulse [148]. Rotating pulses have been observed in a variety of systems, namely in heterogeneous catalysis [149 – 151], electrochemical systems [5, 12, 23] and even in in-vitro heart tissue [152, 153]. In the early 20^{th} century, Lillie [5] reported pulse pattern in transmission of activation of passive metals and it was considered as a model of the protoplasmic or nervous type of transmission. Recently, Lev *et al*. [12] reported a travelling pulse of current density in the electro-dissolution of nickel wires in acidic media. More recently, we observed a spatiotemporal travelling pulse on the Pt ring electrode in the electrocatalytic oxidation of HCOOH [23]. González *et al*. theoretically and experimentally showed resetting and annihilating waves in a ring of cardiac tissue [152, 153].

The direction of motion of the resulting pulses usually depends in a non-trivial way on the initial conditions and/or inhomogeneities of the medium and, thus, often results more from “chance” than from deliberate experimental control. In the normal heart, the control of travelling waves, such as pulse advancement and double pulse reversal, may be effective in the therapy of tachycardia of cardiac tissue [152, 153]. On the other hand, to control the activity (or tolerant passivation) of the electrode by an external electrical stimulus might be effective in running a fuel cell without suffering deactivation of the whole electrode.

In this subsection, experiments and computer simulations of an electrochemical system, where the direction of a pulse can be reversed at will using an external perturbation, will be presented.

4.5.1 Phase resetting by perturbation

We are all familiar with bodily functions such as sleep, breathing, locomotion, heartbeat and reproduction, which depend in a fundamental way on rhythmic behaviours. Such rhythmic behaviours occur throughout the animal kingdom, and a vast literature analyses the mechanisms of the oscillations and how they interact with one another and the external environment. Anyone interested in obtaining an idea of the scope of the inquiry should consult the classic book by A. T. Winfree [154].

It turns out that the mathematical formulation of finite-difference equations has direct applications in the study of the effects of periodic simulation on biological oscillators. The examination of periodic stimulation of biological oscillators involves many difficult issues, both in the biological and mathematical domains, and scientific investigation of these matters is still a research question under active investigation. However, compelling examples of chaotic dynamics in biological systems are found in the periodic stimulation of biological oscillations. Appreciation of the origin of the chaotic dynamics is possible using the material presented so far in this chapter.

Understanding the basics of the periodic stimulation of biological oscillators involves two related concepts: **phase** and **phase resetting**. The phase of an oscillation is a measure of the stage of the oscillation cycle. Because of the cyclicity of oscillations, it is common to represent the phases of the cycles as points on the circle.

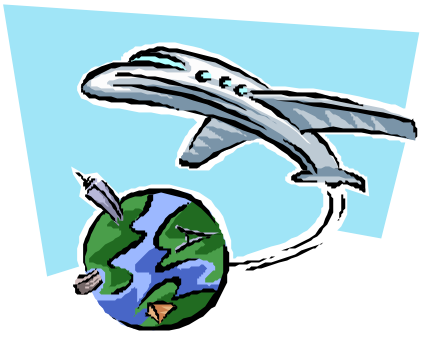

Figure 4.24. Jet travel.

The term “phase resetting” refers to a change of phase that is induced by a stimulus. One example of phase resetting that many people experience is a consequence of jet travel (see Figure 4.24). If you think about travel through different time zones, you will realise that the phenomenon of **jet lag** is associated with a discordance between the phase of your sleep-wake oscillator and the current local time. Staying in the new time zone, the phase resetting takes place in a gradual fashion due to the different light-dark cycles and social stimuli in the new environment.

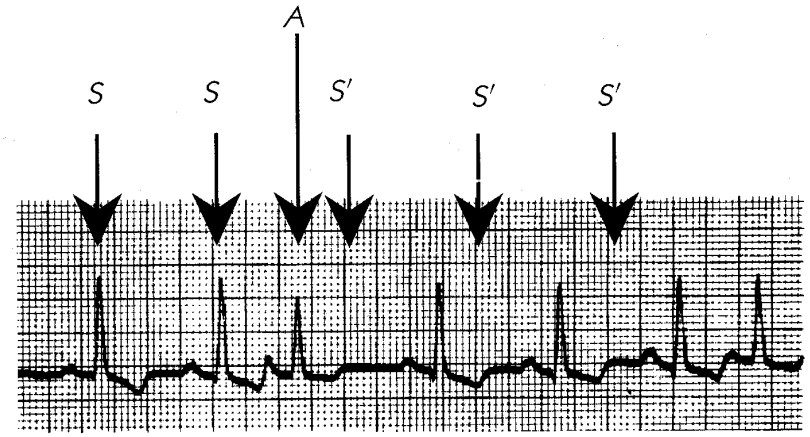

Figure 4.25. Phase resetting in the human heart. The wavey black line is an electrocardiogram – each sharp Λ-shaped spike corresponds to one beat. Those labelled *S* originate in the sine node as normal. The beat labelled *A* originates elsewhere in the atria. In the absence of beat *A*, beats would have occurred at the times labelled *S*’; however, *A* resets the phase of the sine node [155].

More abrupt phase resetting can be induced in many biological systems by appropriately chosen stimuli. For example, the rhythm of the human heart is normally set by a specialised region of the atria called the sine node. However, in some people’s hearts there are extra beats that can interfere with the normal sine rhythm. Sometimes

these extra beats can reset the rhythm. The Figure 4.25 shows an example of an electrocardiograph (ECG) record. The normal sinus beats are labelled *S* and an atrial premature contraction is labelled *A*. If the atrial premature contraction has not occurred, the following sine beat would have been expected at times labelled *S'*. However, the sine firing is reset by the atrial premature stimulus, leading to a sine beat at a different time than would presumably have occurred without the atrial premature contraction.

Since it is difficult to study the effects that electrical stimuli have on the heart, experimental preparations have been developed that enable detailed analysis [156, 157]. Figure 4.26 shows phase resetting of spontaneously oscillating cardiac tissue derived from embryonic chicken hearts. The upward deflections are called **action potentials** and are associated with the contraction cycle of the chicken heart cells. The intrinsic length of the heart cycle is T_0. The sharp spike delivered after a time interval of d after the onset of an action potential is an electrical stimulus delivered to the aggregate. The stimulus phase resets the rhythm so that following the stimulus the new cycle length is T (rather than T_0). Experimental studies show that the magnitude of phase resetting depends on both the amplitude of the stimulus and the phase of the cycle at which the stimulus is delivered.

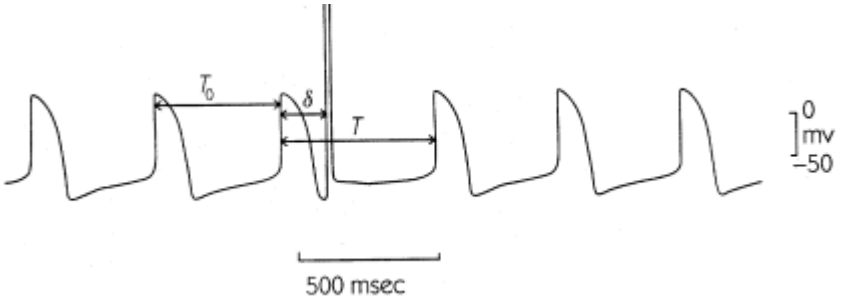

Figure 4.26. Recording of transmembrane voltages from spontaneously beating aggregates of embryonic chicken heart cells. The intrinsic cycle length is T_0. A stimulus delivered at a time d following the start of the third action potential leads to a phase resetting so that the subsequent action potential occurs after time T. After this, the aggregate returns to its intrinsic cycle length [156].

4.5.2 Experimental setup for external perturbation

Eleven reference electrodes were distributed at about 0.3 mm distance from the WE in order to monitor the local potential, while at the 12th position a Pt wire (*ca.* 1 mm from WE) served as external trigger (see [21] for details of the experimental setup). The electrolyte was 0.1 M HCOONa/0.033 M H_2SO_4, to which 1×10^{-6} M $Bi(ClO_4)_3$ was added, which leads to a substantial increase of the electrocatalytic activity of Pt toward formic acid oxidation.

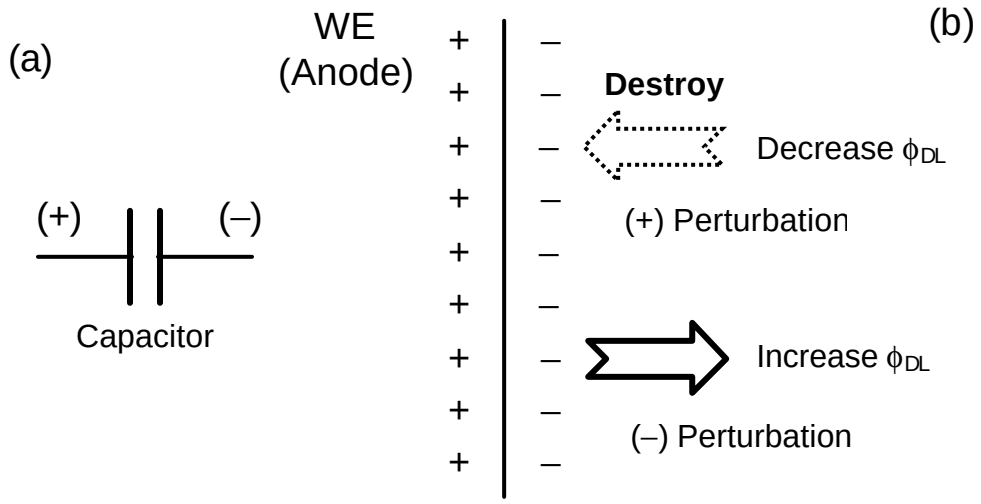

Figure 4.27. (a) A capacitor and (b) the metal-solution interface as a capacitor with positive charge on the Pt electrode. In Figure (b), the principle of positive perturbation in the electrochemical oxidation of formic acid on Bi/Pt electrode was schematically described (see text for the details).

Since charge cannot cross the ideally polarised electrode interface when the potential across it is changed, the behaviour of the electrode/solution interface is analogous to that of a capacitor. A capacitor is an electrical circuit element composed of two metal sheets separated by a dielectric material (Figure 4.27(a)). The electrode/solution interface has been shown experimentally to behave like a capacitor, and a model of the interfacial region somewhat resembling a capacitor can be given. At a given potential, there will exist a charge on the metal electrode and a charge in the solution (see Figure 4.27(b)). Whether the charge on the metal is negative or positive

with respect to the solution depends on the potential across the interface and the composition of the solution. In the electro-oxidation of formic acid on Bi/Pt electrode, a positive perturbation was applied in order to investigate the change of the interfacial potential response along the ring Pt anode. For a reference, the interfacial potential can be decreased locally by applying positive perturbation, while negative perturbation can increase the double layer potential (ϕ_{DL}), as shown in Figure 4.27(b).

4.5.3 Travelling pulse reversal

Experimental observations

On the anodic scan during the cyclic voltammetry of the Pt ring electrode in formic acid solution, potentiostatic current oscillations were obtained in a potential range from about + 110 mV to + 280 mV, as shown in Figure 4.9(a). Due to the proximity of the RE to the WE, no in-phase oscillations were possible; rather, anti-phase spatiotemporal oscillations developed in the form of standing waves or rotating pulses [22, 23].

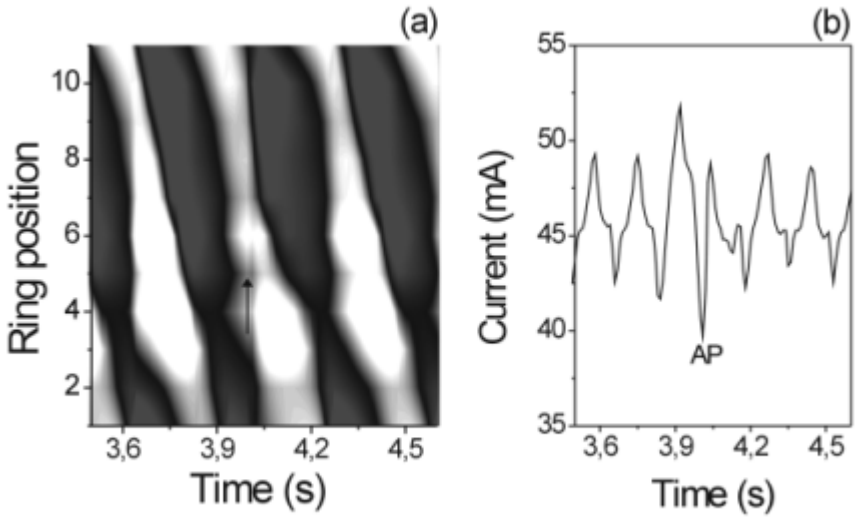

Figure. 4.28. Phase resetting of a rotating pulse due to a locally activating perturbation of + 1 V and 200 ms applied at position 12. (a) Spatiotemporal contour plot (black: active state, white: passive state) and (b) temporal current oscillation. AP: activating perturbation.

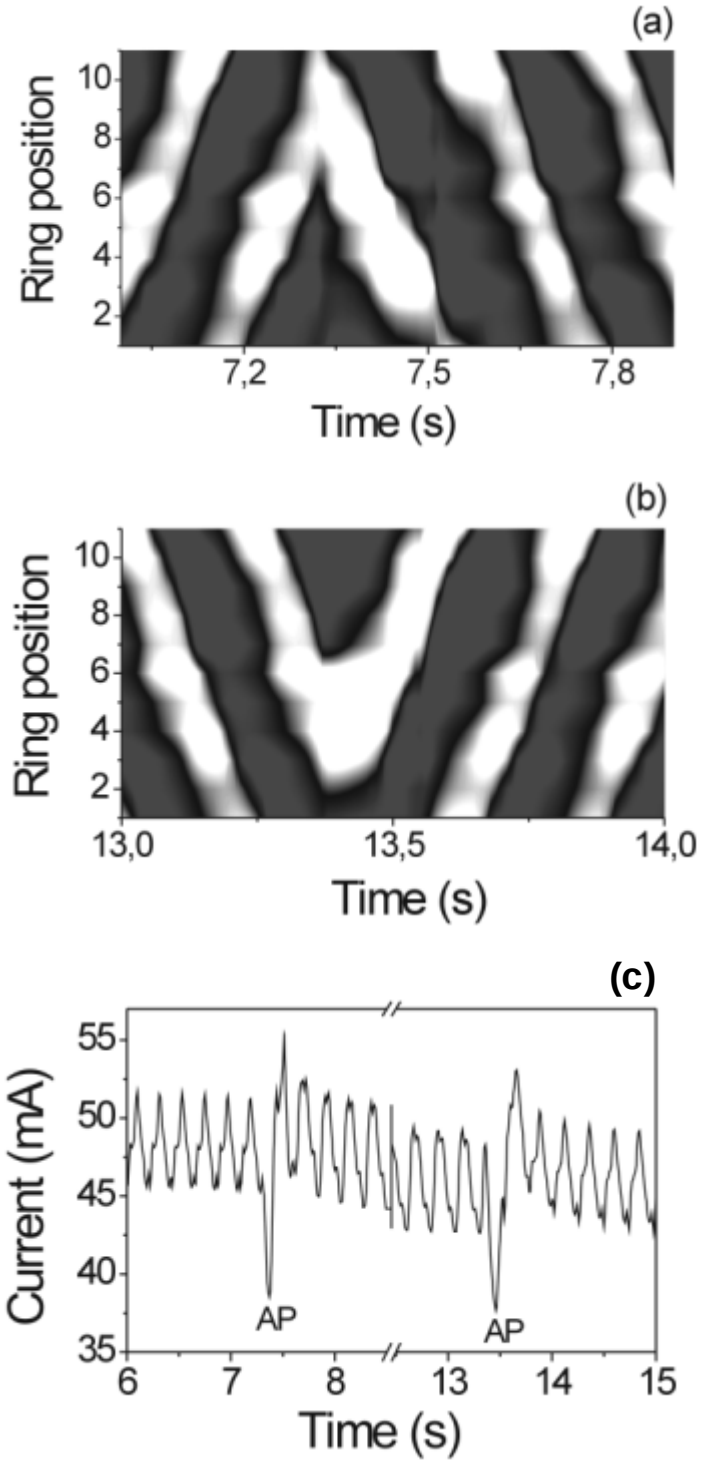

Figure 4.29. Double reversal of a rotating pulse due to a locally activating perturbation of +2 V and 200 ms applied at position 12. (a) and (b) Spatiotemporal pattern (black: active state, white: passive state) and (c) the resulting current oscillations.

A rotating pulse was subjected to a pulse-shaped perturbation of usually 200 ms duration. For small trigger amplitudes (≤ 1.0 V), no pulse reversal was obtained, rather the pulse rearranged in the same direction with its phase advanced or retarded compared with what it would have been without the perturbation. An example is shown in Figure 4.28. Thus, the response resembled the well-known phase resetting behaviour of limit cycles for small perturbations (see [154, 158]). As already mentioned in section 4.5.1, phase resetting refers to a change of phase that is induced by a stimulus (here pulse perturbation) and it can be induced in many systems by appropriately chosen stimuli.

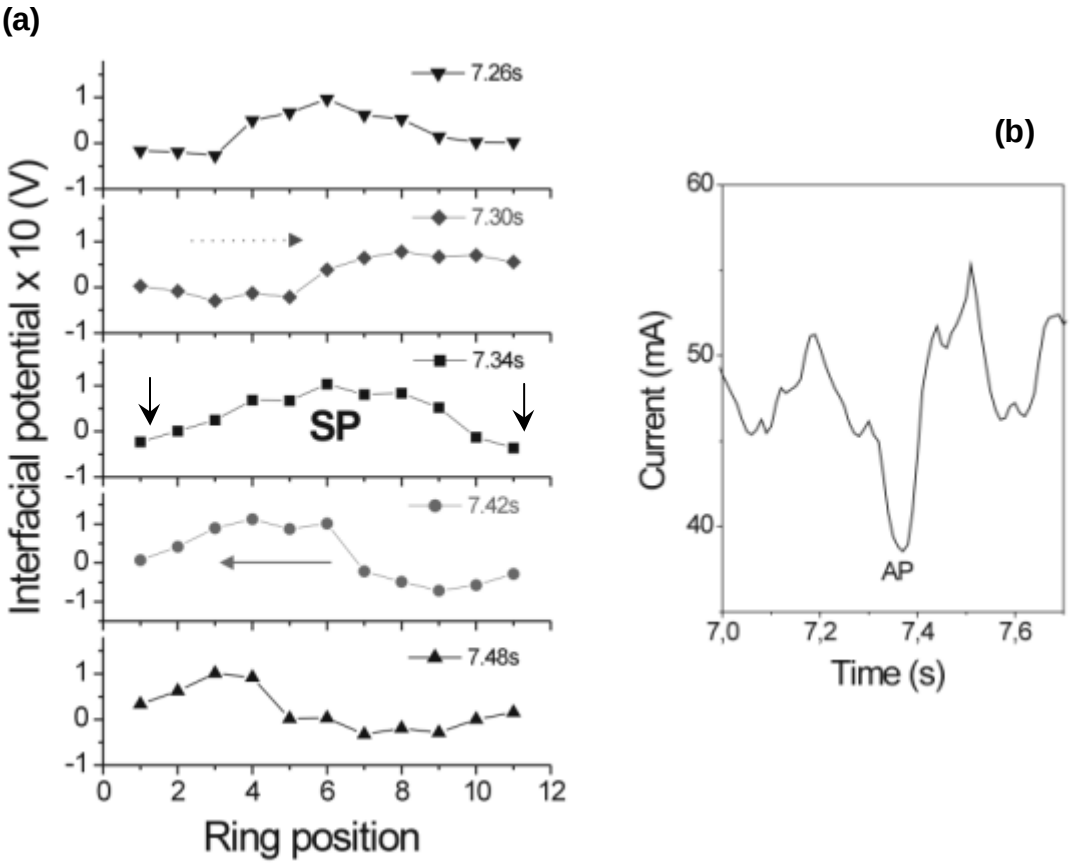

Figure 4.30. (a) Temporal sequence of reversal behaviour of a rotating pulse due to a locally activating perturbation (AP) of + 2 V and 200 ms applied at position 12. The two arrows at t = 7.34 s indicate activating perturbation. (b) Temporal current oscillations.

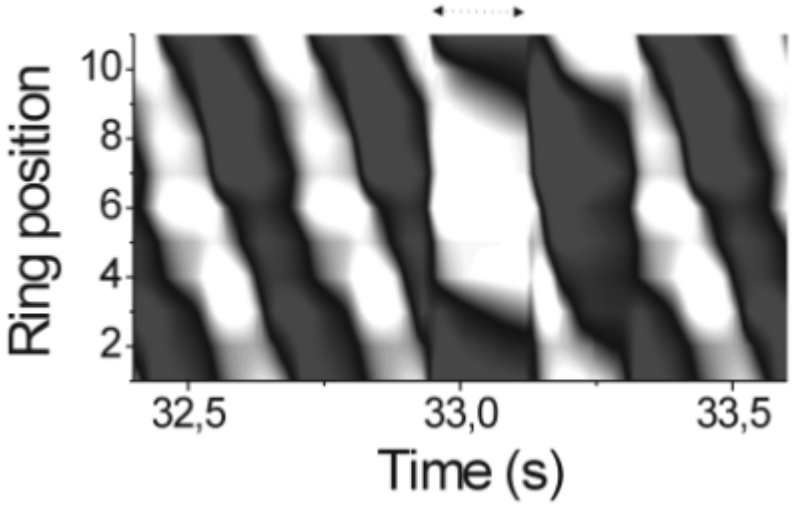

Figure 4.31. Critical slowing down (dotted arrow) of a rotating pulse due to a locally activating perturbation of + 1 V and 200 ms applied at position 12.

The situation changed significantly for higher perturbation amplitudes ($\geq$ 2 V). Regarding the pulse as an active (high-current) zone on an otherwise passive (low-current) electrode, a perturbation in front of the pulse led to pulse advancement, whereas perturbing behind it resulted in a reverse of direction. This is shown in Figures 4.29 and 4.30, where a clockwise travelling pulse and an anti-clockwise direction induced by two subsequent perturbations. On an ideal electrode the total current I (Figure 4.28(b) resp. Figure 4.29(c)) would be constant during pulse rotation. However, due to inhomogeneities of the ring electrode, it exhibits characteristic oscillations which repeat every period. For a given electrode the location of the pulse on the ring could thus be assessed indirectly without necessity of real-time spatiotemporal measurements. Note that the pulse orientation was also visible from the integral current (see Figure 4.29(c)), *i.e.*, at least some inhomogeneities were asymmetric.

For phase shifts around zero (perturbation right on the pulse), the pulse appeared stationary for some time before starting to move again, as shown in Figure 4.31 (“critical slowing down” marked with dotted line).

Theoretical simulations

Computer simulations [27, 159] were carried out by J. Christoph using a reaction-migration system with the double layer potential φ (x, t) as a fast variable and a chemical species c (x, t) as a slow variable with time scale ε.

$$C_{dl}\partial_t\varphi = -i_{reac}(\varphi, c) + \frac{U-\varphi}{R} + \kappa \int_0^{2\pi} H(|x - x'|)[\varphi(x') - \varphi(x)]\,dx', \qquad (4.5)$$

$$\partial_t c = \varepsilon(-i_{reac}(\varphi, c) + 1 - c) \quad \text{where} \quad i_{reac}(\varphi, c) = ck(\varphi). \qquad (4.6)$$

Here C_{dl} denotes the double layer capacity, i_{reac} the local faradaic current density, U the outer applied potential, R the total resistance and κ the conductivity of the electrolyte. At the heart of the spatial integral coupling lies the spatial coupling function $H(|x - x'|)$ which represents the coupling between two points x and x' along the WE. Due to the symmetry of the ring geometry, *H* is simply a function of the distance x– x' between two points. For the geometry in question (ring as WE with RE in the centre), *H* falls off with distance and becomes negative on the opposing side of the ring (for details of the derivation of *H* from potential theory and its exact shape see [14, 21, 27]).

Figure 4.32 is the schematic diagram of pulse reversal by applying an activation pulse on ring position 12. A pulse is initially travelling from phase 0 to 2π. Higher and lower interfacial potentials indicate passive and active states, respectively. If one applies a positive pulse near before π, a pulse reversal pattern can be obtained. On the other hand, when an activation pulse is applied after π, only a pulse advancement (uni-directional pulse) can be observed.

Figure 4.33 reproduces computer simulations of pulse advancement (a) and pulse reversal (b) occurring when the perturbation was applied at different phases. As in experiment, the perturbation has to exceed a threshold so that reversal can occur. The above phenomena can be rationalised in terms of the nonlocal nature of migration coupling.

The activating trigger acts most strongly locally, but also nonlocally everywhere on the electrode, the perturbation strength at other places being determined by the

coupling function $H(x, x')$, which effect in particular causes passivation on the opposite side.

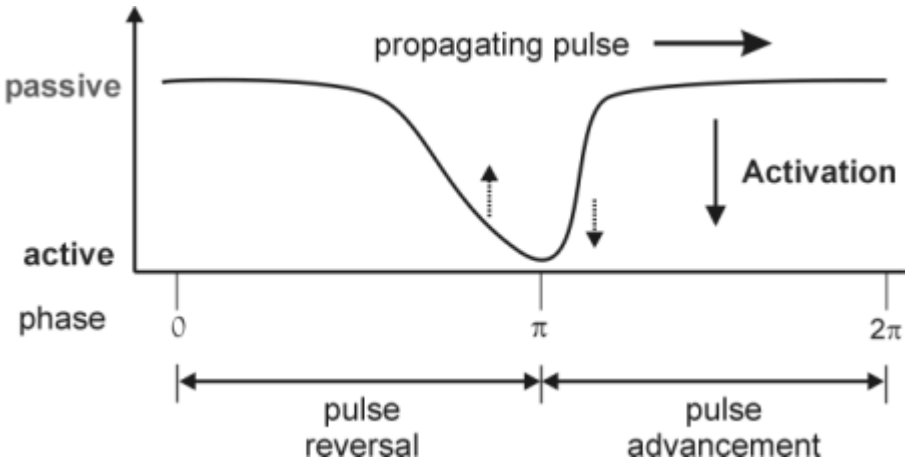

Figure 4.32. Schematic diagram of pulse reversal depending on the position of applied optimal perturbation.

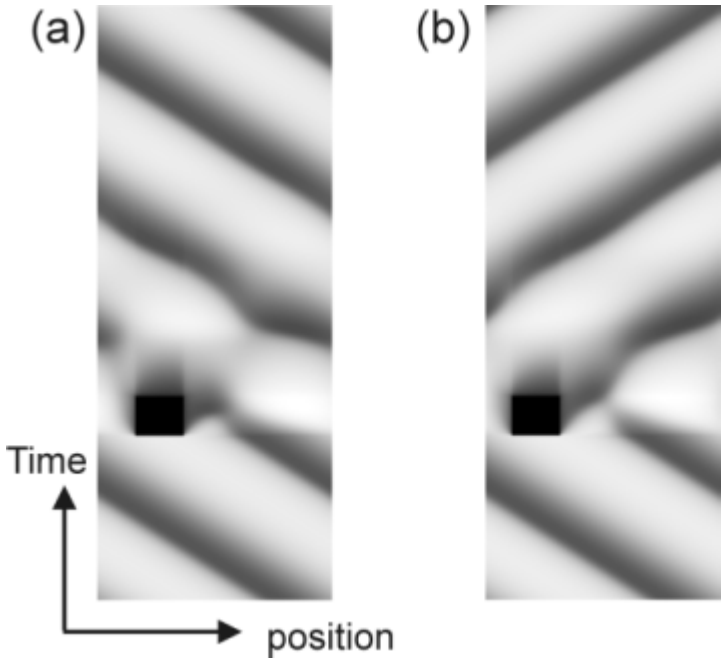

Figure 4.33. Theoretical simulation of controlled pulse patterns. (a) Pulse advancement and (b) pulse reversal. Courtesy of J. Christoph [159].

For small perturbation amplitudes, the local activation predominates leading to standard phase resetting. At higher amplitudes the remote passivation also becomes important. Consequently, a perturbation behind a pulse will cause the local current to increase behind, but decrease in front of the pulse. This is exactly opposite to the natural (unperturbed) current gradients on both sides of the pulse, *i.e.*, it must change its direction of motion. The described behaviour is expected in general for systems that combine short-range activation with long-range inhibition coupling.

4.6 Spatiotemporal patterns with increasing distance of the reference electrode (RE)

4.6.1 Pattern sequence with various b at a fixed potential

The distance parameter β at a ring-shaped electrode is defined as the distance between ring working electrode and the reference electrode divided by the outer radius of the working ring electrode:

$$ß = \frac{D_{RE-WE}}{R_{OR}}, \tag{4.7}$$

where D_{RE-WE} is the distance between RE and WE and R_{OR} is the outer radius of the working ring electrode.

Christoph calculated the coupling function H of the ring electrode for various values of β. In Figure 4.34, the sign of the coupling function H strongly depends on the position of the reference electrode. For small β, H becomes negative for large distances $|x - x'|$. Thus, this can induce anti-phase inhomogeneous patterns. However, the coupling function of all positions on the ring will be positive when the RE is placed far away from the WE (*i.e.*, at large β).

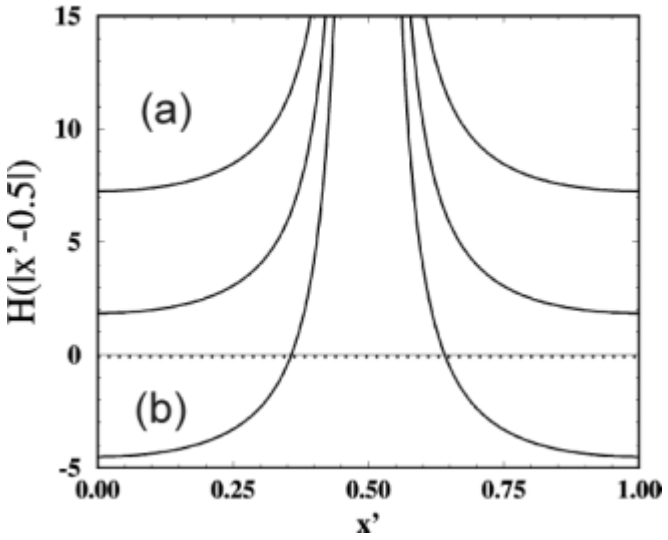

Figure 4.34. Dependence of the coupling function *H* on parameter β for the reference point located at x= 0.5. For large β (a), *H* represents a positive nonlocal coupling. For small β (b), a negative nonlocal coupling, that is a positive short-range and negative long-range coupling, arises. Courtesy of J. Christoph [27].

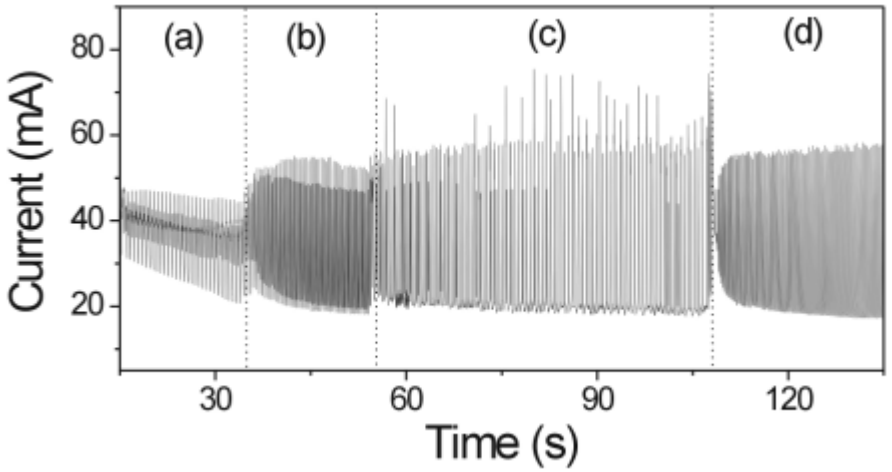

Figure 4.35. Chronoamperometric profile with different values of β when constant outer potential of + 170 mV on the positive going scan is applied. (a) β = 0, (b) β = 0.25, (c) β = 0.50 and (d) β ≥ 0.7.

We found potentiostatic current oscillations in a potential range from + 110 mV to + 280 mV at $\beta = 0$ (see Figure 4.9(a)). The distance (D_{RE-WE}) was manually changed to investigate different pattern formation of the interfacial potential with different β. Figure 4.35 shows different temporal current oscillations at $\beta = 0.0$, $\beta = 0.25$, $\beta = 0.5$ and $\beta \geq 0.7$ at a fixed outer potential (U) of + 170 mV. The spatiotemporal pattern sequence of the interfacial potential is reproduced in Figures 4.36, 4.37 and 4.38.

Figures 4.36(a) and 4.36(b) are current-time profile and the space-time plot of the rotating pulse on the ring when the reference electrode is placed on the same vertical position of the working electrode (*i.e.*, $\beta = 0$). The rotating pulse pattern is formed due to the negative nonlocal coupling (see II marked in Figure 4.34). Periodic current oscillations with an oscillatory frequency of 6 Hz are observed, and an activation pulse (white colour domain) is circling the ring of at the same rate.

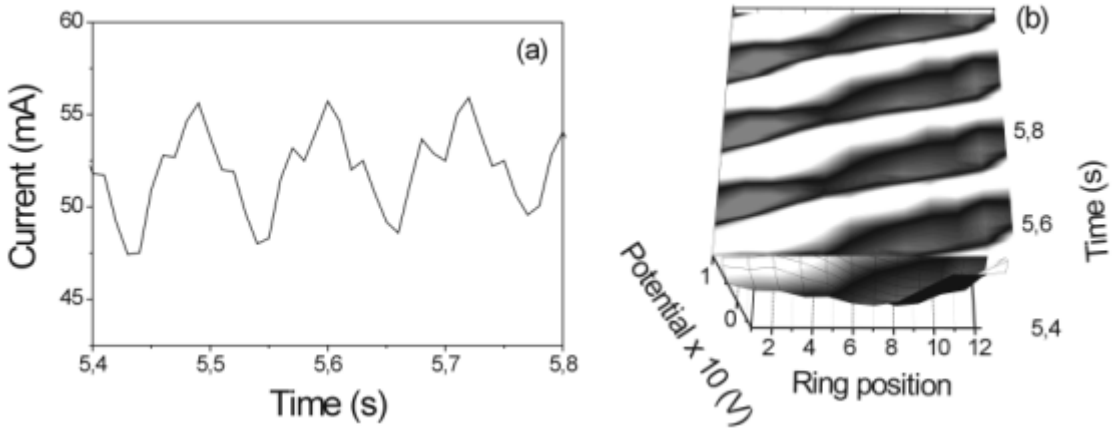

Figure 4.36. Experimental observations of inhomogeneous oscillations at $\beta = 0$. (a) Temporal oscillations and (b) travelling pulse pattern.

At $\beta = 0.25$, we observed defect-mediated standing waves (*DSW*) in Figure 4.37, also due by the negative nonlocal coupling. A surface defect located near ring positions 3 and 4 resulted in propagation failure of the travelling pulse. Thus, the pattern observed looks like standing waves. Since the complex pattern formation was observed at $\beta = 0.50$ (see Figure 4.38), further experiments and theoretical simulations are necessary and are in progress.

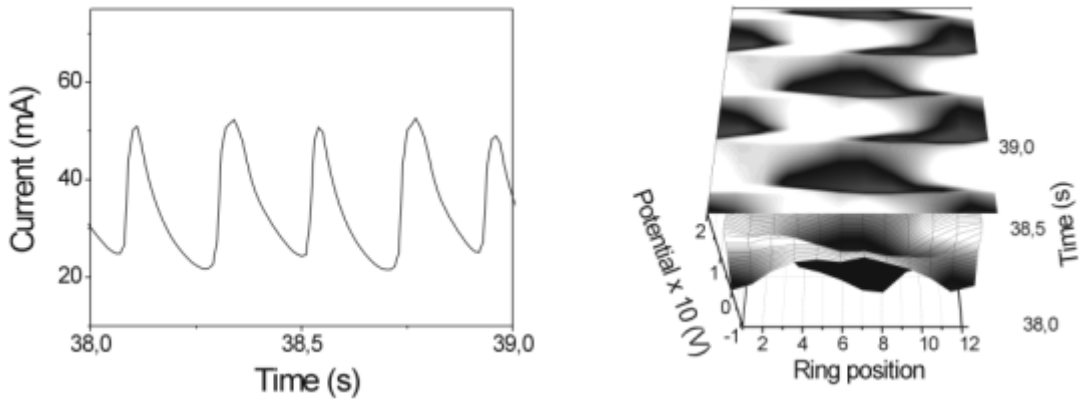

Figure 4.37. Spatiotemporal observations of inhomogeneous oscillations at β = 0.25.

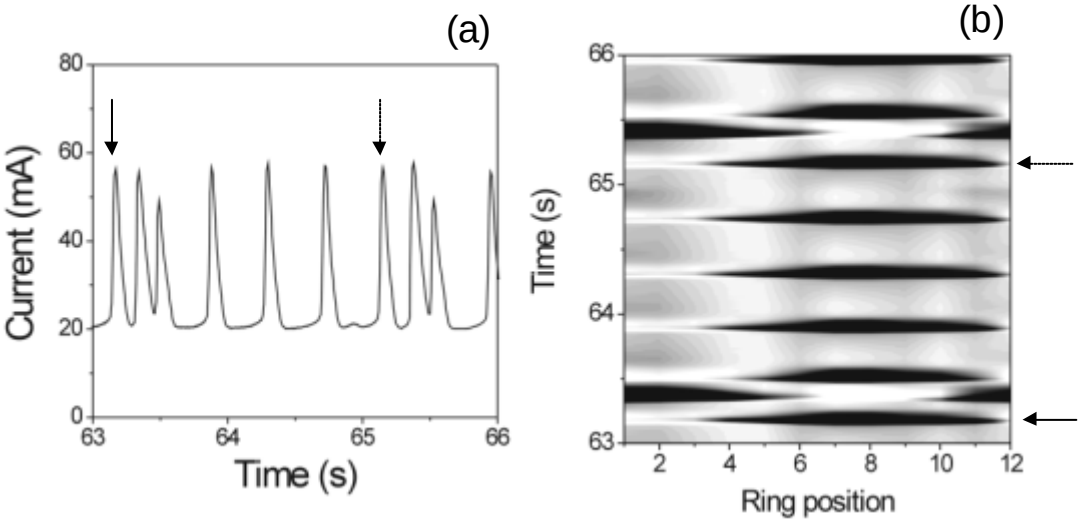

Figure 4.38. (a) Current curves and (b) complex spatiotemporal pattern at β = 0.5.

In-phase oscillations were obtained, when β was equal to or higher than 0.7. Figure 4.39(a) shows the relaxation current oscillations. Figure 4.39(b) is the 2D plot of the spatiotemporal behaviour and white and black colours represent active (*a*) and passive (*p*) states, respectively. We find the homogeneous oscillations, certainly due to the positive global coupling. All positions on the ring have the same value of the interfacial potential at the same time. The experimental value for homogeneous oscillations of 0.7 is in good agreement with calculations by J. Christoph, who showed that for $\beta \geq 0.6$ the electrode is expected to become homogeneous [27].

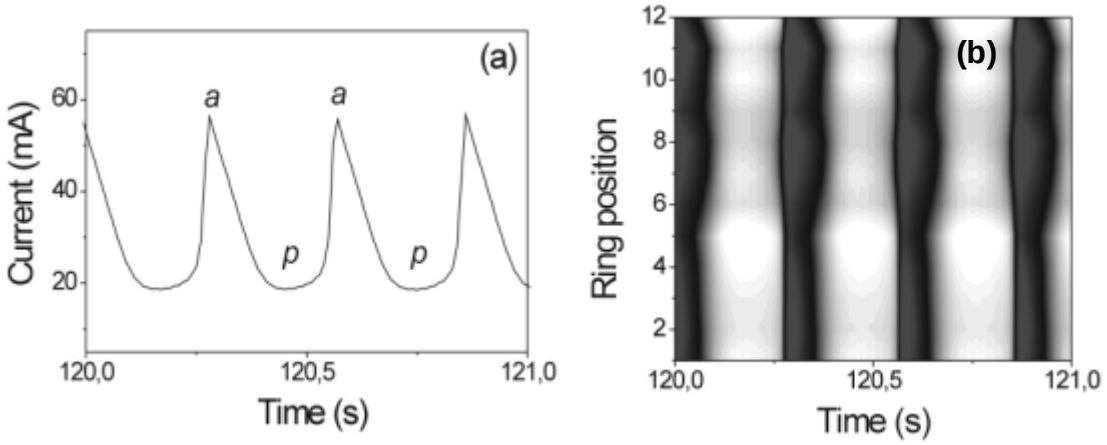

Figure 4.39. Experimental observations of in-phase homogeneous oscillations at $\beta \geq 0.7$. (a) Temporal behaviour of relaxation current oscillations and (b) spatiotemporal pattern of in-phase oscillations.

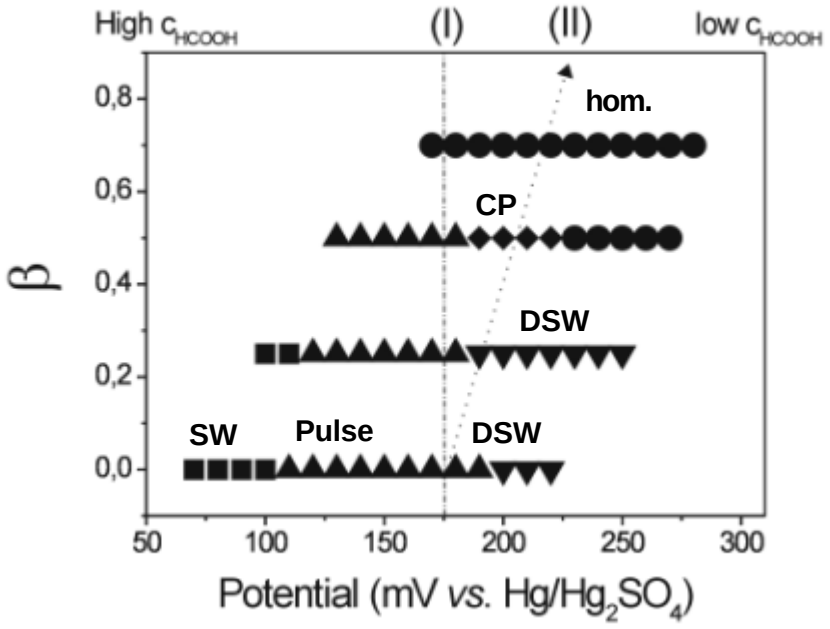

Figure 4.40. Map of spatiotemporal pattern formation with different β and outer potential. *SW*: standing waves, *Pulse*: travelling pulse, *DSW*: defect-mediated standing waves, *CP*: complex patterns, *hom.*: homogeneous oscillations.

4.6.2 Spatiotemporal pattern map at various b

Figure 4.40 is the map of the spatiotemporal patterns of the interfacial potential measured by cyclic voltammetry at different values of the parameter β. According to the map, one can expect that a travelling pulse might be the prevailing pattern when an outer potential of + 170 mV is constantly applied, which means that the observed pattern at $\beta = 0.25$ and 0.5 should be a pulse. However, we find the different pattern sequences, travelling pulses, *DSW*, complex patterns and in-phase oscillations in the above Figures 4.36, 4.37, 4.38 and 4.39.

The concentration of formic acid on the surface decreases as a function of time in the absence of stirring. Thus, the experiments of constant U do not really represent a vertical line, but rather induce a slight shift to the right (as indicated by line II in Figure 4.40).

4.7 Defect-mediated spatiotemporal mixed-mode oscillations

The theory of nonlinear dynamics offers powerful tools for the analysis of experimentally observed complex phenomena exhibited by dissipative systems held far from equilibrium. In the 1980s, several studies concentrated on temporal behaviour consisting of large and small oscillations with a substantial range of intermediate amplitudes unrealised [160 – 164]. This oscillatory phenomenon is referred to as mixed-mode oscillations (MMOs). Most sequences of different MMOs identified can be assigned to one of two classes: (a) periodic-chaotic sequences, in which intervals of periodicity are separated by an interval of chaotic states which resemble random mixtures of the adjacent periodic patterns, and (b) Farey sequences, which we define as periodic sequences for which a one-to-one correspondence with an ordered sequence of rational numbers can be established.

Hudson *et al*. [165, 166] first observed periodic-chaotic sequences in the Belousov-Zhabontinskii (BZ) reaction. Swinney and Maselko [160, 161] revealed a

Farey sequence of MMOs. Farey sequences are familiar in periodically forced systems where periodic states are associated with locking of the driving frequency with an intrinsic frequency of the autonomous system. In a broader perspective, mixed-mode behaviour has been extensively studied within a nonlinear dynamics context. Albahadily *et al.* [164, 167] first reported similar behaviour for copper electro-dissolution in phosphoric acid, which is compared with similar occurrences reported for the Belousov-Zhabotinskii (BZ) reaction [161]. In the electrochemical system, the MMOs scenario arises *via* a different nonlinear mechanism than the one proposed for the BZ reaction (locking on a torus). Ringland *et al.* [168] proposed a family of one-dimensional two-extremum maps as a limiting representation of the basic structure in phase-space that supports MMOs. The proposed mapping exhibits a spectrum of one-parameter sequences of MMOs, thus offering a strong basis for unification of the broad range of qualitatively different reported experimental observations of MMOs. Koper *et al.* [169, 170] proposed a simplified three-dimensional model of electrochemical MMO processes taking place at rotating electrodes. The focus to date was on a set of states in which each member consists of a different combination of large and small temporal mixed-mode oscillations (TMMOs).

In this section we first describe spontaneous spatiotemporal data of a complex nonlinear scenario (spatiotemporal mixed-mode oscillations, SMMOs) observed during the potentiostatic oxidation of HCOOH on Pt deposited by Bi. A set of SMMOs which can be put in one-to-one correspondence with an ordered set of rational numbers will be presented.

In the electrocatalytic oxidation of HCOOH on Bi/Pt electrode, potentiostatic current oscillations in a potential range from + 110 mV to + 280 mV (see Figure 4.9(a)) were observed. At the termination of current oscillations on the anodic scan during the cyclic voltammetry, spontaneous pulse reversal behaviour was observed. Thus, the potential was kept constant in order to measure travelling pulse reversal behaviour as a function of time (chronoamperometry). Measured oscillations representing many spatiotemporal mixed-mode states (SMMOs) are shown in Figures 4.41, 4.42, 4.43 and 4.44.

The clear dichotomy between active pulse reversal and uni-directionally travelling pulse (uni-pulse) enables one to characterise a periodic state by listing the length of unbroken stretches of uni-pulse and reversed pulse in one period. In other

words, for compactness, the periodic (non-chaotic) states using the notation P^R, where P is the uni-directional pulse and R the pulse reversal on the ring of the particular spatiotemporal mixed-mode behaviour. This abbreviated notation is standard in the description of SMMOs. Thus, the list P_1, R_1, P_2, R_2, which could be written for clarity in the form $P_1^{R1} - P_2^{R2}$, denotes a state whose cycle consists of P_1 uni-pulses followed by R_1 pulse reversals, followed by P_2 uni-pulses, followed by R_2 pulse reversals.

The SMMOs shown in Figures 4.41, 4.42, 4.43 and 4.44 indicate that the ratio of uni-pulse to pulse reversal steadily decreases with time.

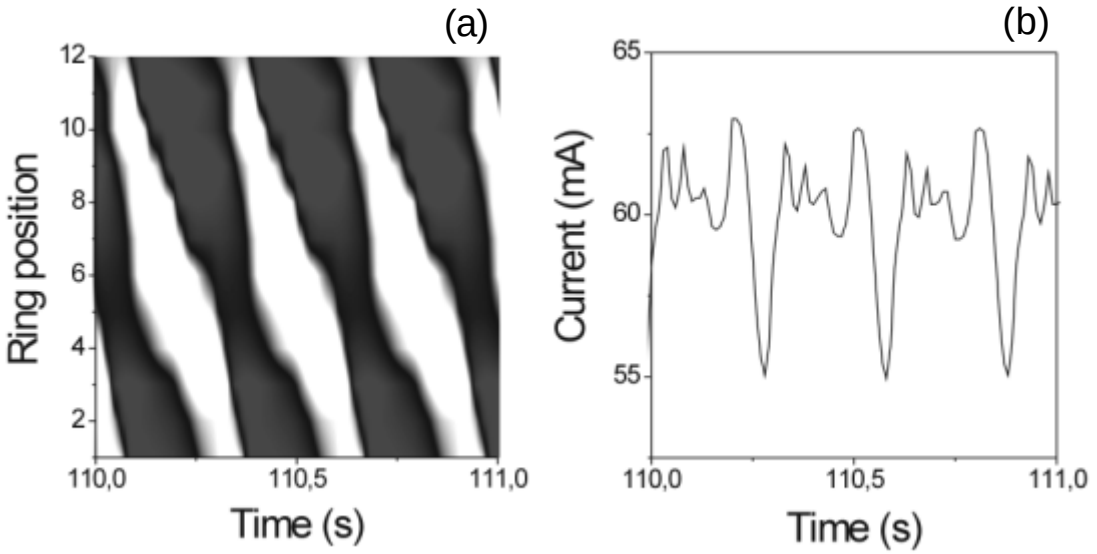

Figure 4.41. (a) Spatial and (b) temporal oscillations of uni-pulse (always travelling with one direction along the ring; clockwise or counter-clockwise) during the potentiostatic oxidation of HCOOH on Bi/Pt ring electrode ($P^R = 1^0$). Black and white colours indicate active and passive states of the electrode, respectively.

Figure 4.41 presents spatiotemporal oscillations of 1^0 (P^R). A counter-clockwise active travelling pulse of interfacial potential is obtained along the ring. In Figure 4.41(b), asymmetric current oscillations, *i.e.*, little spikes in one period, are observed, and they are clearly seen in the spatiotemporal behaviour. Between positions 3 and 7 the system is more passive (white domain) than at other positions. From the sequence observed in Figure 4.41 and forthcoming Figures 4.42, 4.43 and 4.44, the sequence can be characterised as a Farey tree. The Farey ratio in this case is defined as the ratio of

uni-pulse to pulse reversal for a given type of behaviour. For example, in Figure 4.41 we observed at high values of the current a state composed of only pulse travelling (1^0 SMMOs, *i.e.*, Farey ratio infinity).

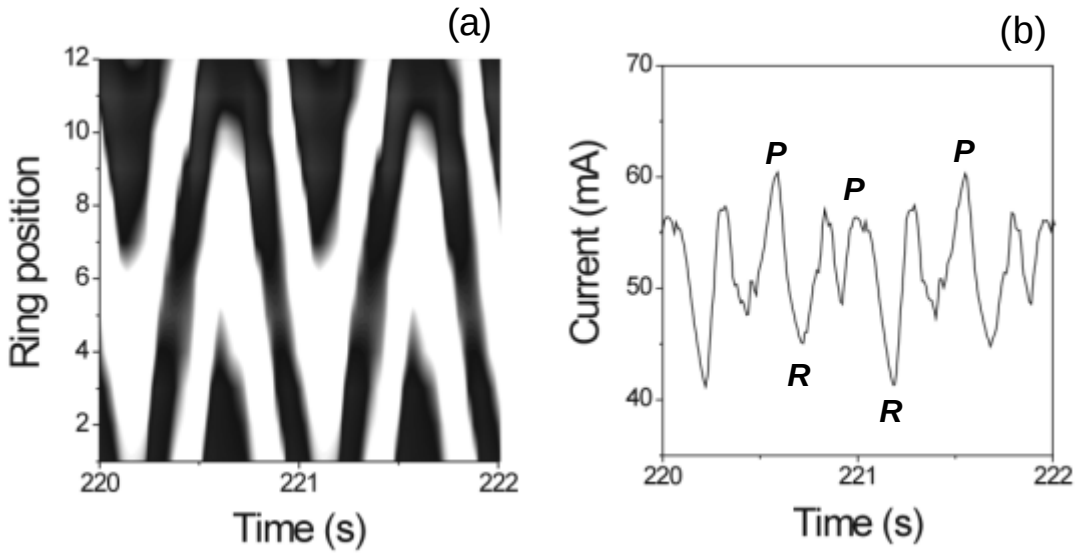

Figure 4.42. (a) Spatial and (b) temporal mixed-mode oscillations of pulse reversal. The interfacial potential (ϕ) is measured with respect to a WE ring electrode ($P^R = 1^1$). Black and white colours indicate active and passive states of the electrode, respectively. ***P*** is uni-pulse and ***R*** is pulse reversal.

We first observe the behaviour consisting of one active uni-pulse followed by one pulse reversal, and it is a 1^1 SMMOs (*i.e.*, Farey ratio 1), as shown in Figure 4.42(a). This spatiotemporal pattern is clearly observed in temporal current oscillations (see ***P*** and ***R*** in Figure 4.42(b)). The state consisting of one uni-pulse followed by two pulse reversals (a 1^2 SMMOs, Farey ratio 1/2), one uni-pulse followed by three pulse reversals (a 1^3 SMMOs, Farey ratio 1/3) and one uni-pulse followed by six pulse reversals (a 1^6 SMMOs, Farey ratio 1/6) were subsequently also obtained (see Figure 4.43). During the experiments, we were also able to locate pure pulse reversals (0^1 SMMO) as shown in Figure 4.44.

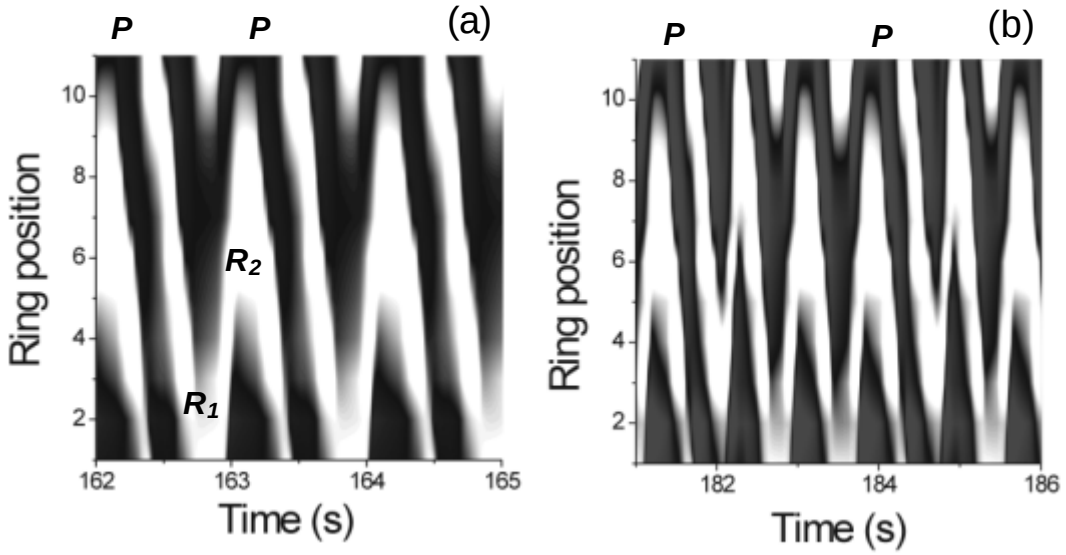

Figure 4.43. Spatiotemporal patterns of (a) $P^R = 1^2$ and (b) $P^R = 1^6$ in the electro-oxidation of HCOOH on Bi/Pt surface ($P^R = 1^3$ not shown in this Figure). Black and white colours indicate active and passive states of the electrode, respectively. ***P*** is uni-pulse and ***R*** is pulse reversal.

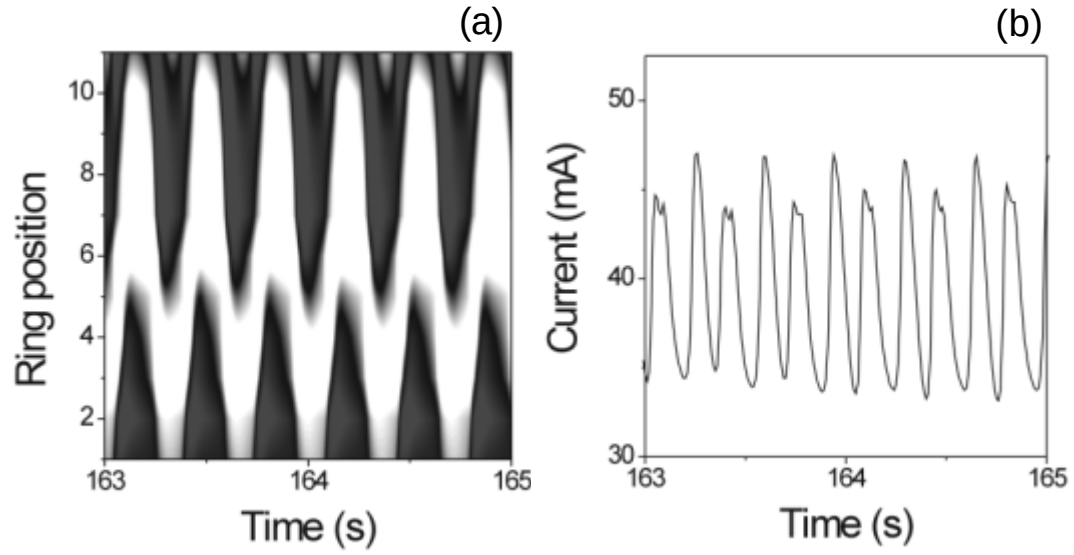

Figure 4.44. (a) Spatial and (b) temporal mixed-mode oscillations of pulse reversal ($P^R = 0^1$) without any uni-direction pulse.

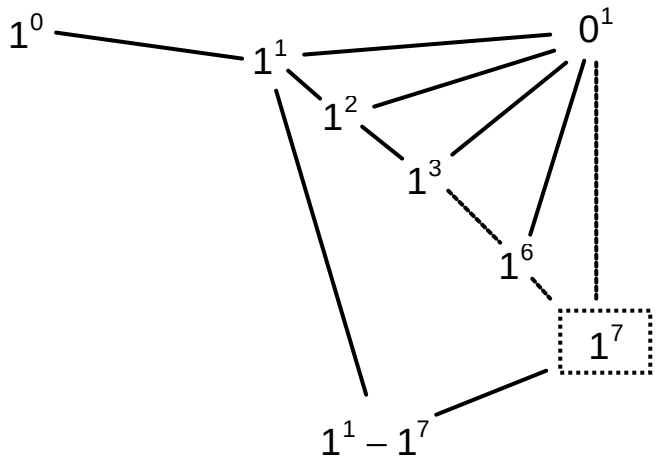

Figure 4.45 A portion of the Farey tree constructed of observed states. The state 17 was not obtained in experiment, though $1^1 - 1^7$ was.

The Farey tree arises in number theory as an illustration of a scheme for the progressive generation of all the rational numbers between a given pair of rationals. This operation is known as Farey addition: the Farey sum of two rationals a/c and b/d is (a + b)/(c + d); the ratios of the numerators and denominators are summed separately. The two starting rationals are written down at opposite sides of the page, and then each state of the process consists of writing their Farey sum between each pair of adjacent already-written numbers. A construction analogous to Figure 4.45 follows if we spread the numbers out in the vertical dimension and draw a line segment from each number to both of its **parents**.

In Figure 4.45 the spatiotemporal pulse reversal observed was listed. The list is laid out on an incomplete **Farey tree**, which manifests the relationships that exist among the states. It is seen that the pattern of each state is the concatenation of the patterns of a pair of states above it, one on either side. The state characterised by $1^1 - 1^7$ was the most complicated SMMO that could be reliably reproduced in experiment. Before the transition to the 0^1 state, in each experimental run sequences $1^1 - 1^n$ with n = 10…30 were also obtained, but those were never stable (usually only 1 period was obtained) and may actually have been due to parameter noise rather than being genuine attractors of the system. Examples are shown in Figures 4.46 and 4.47.

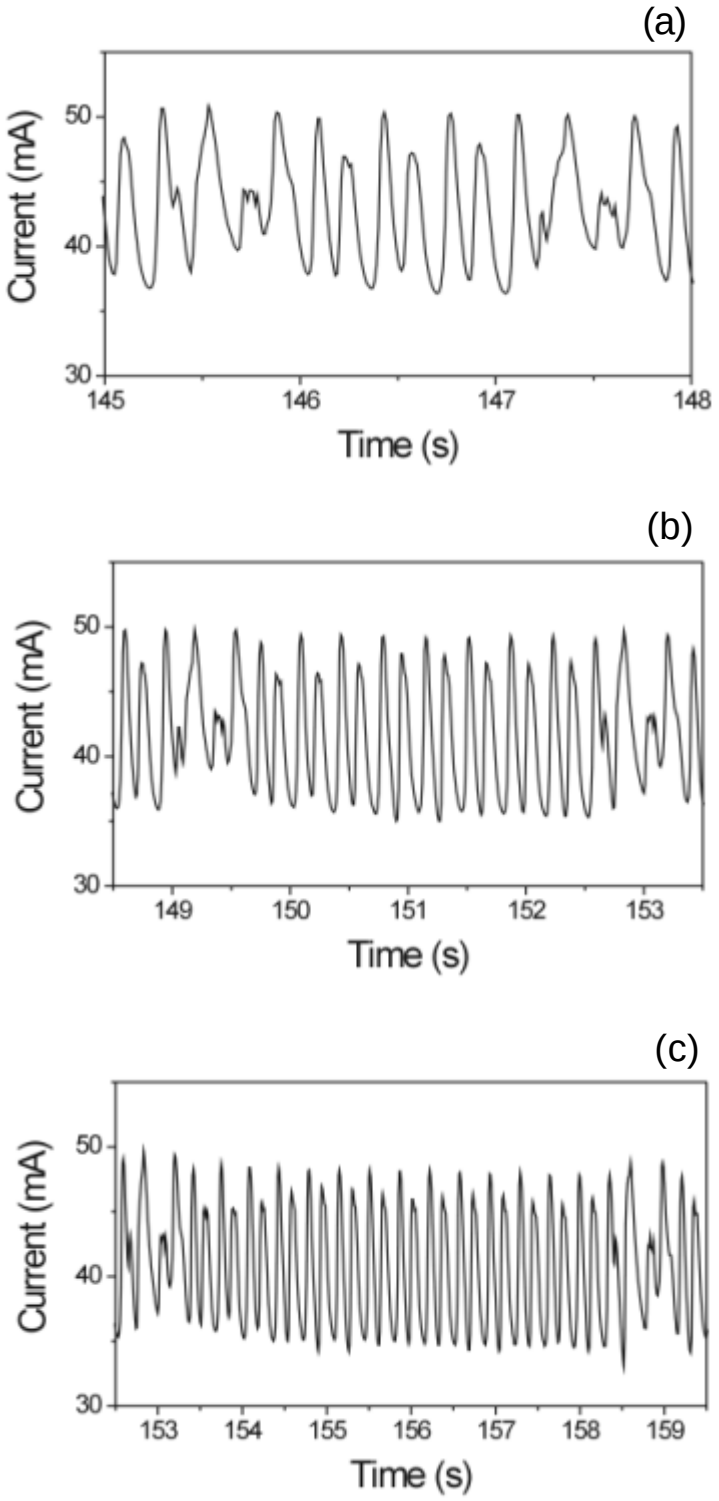

Figure 4.46 Complex temporal mixed-mode oscillations (TMMOs).

(a) $P_1{}^{R1} - P_2{}^{R2} = 1^1 - 1^7$, (b) $P_1{}^{R1} - P_2{}^{R2} = 1^1 - 1^{17}$ and

(c) $P_1{}^{R1} - P_2{}^{R2} = 1^1 - 1^{29}$. Experimental conditions are the same as Figure 4.41.

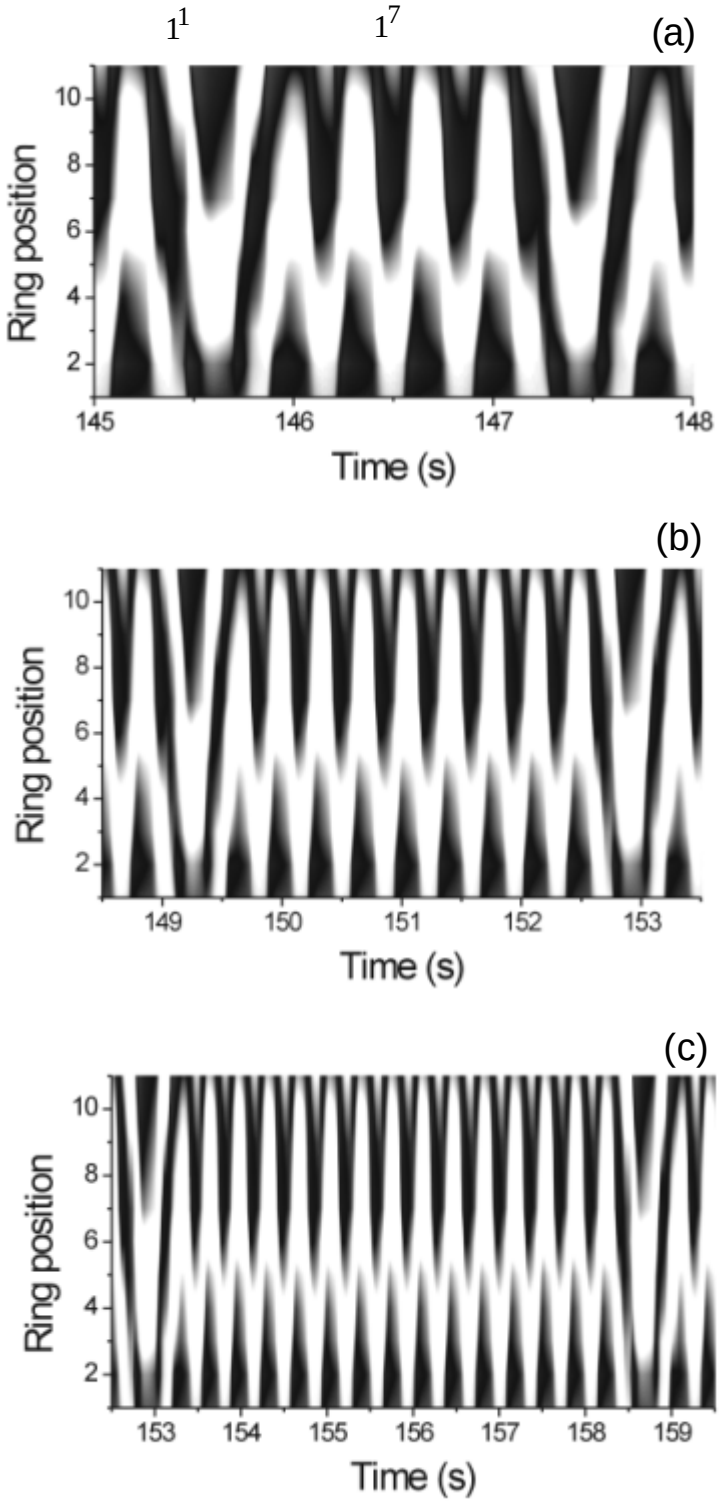

Figure 4.47 Complex spatiotemporal mixed-mode oscillations (SMMOs) of pulse reversal. (a) $P_1{}^{R_1} - P_2{}^{R_2} = 1^1 - 1^7$, (b) $P_1{}^{R1} - P_2{}^{R2} = 1^1 - 1^{17}$ and (c) $P_1{}^{R1} - P_2{}^{R2} = 1^1 - 1^{29}$ in the electro-oxidation of HCOOH on a Bi-modified Pt electrode. $\beta = 0.25$.

4.8 Summary

In the oxidation of formic acid on Bi/Pt, temporal periodic recovery of the activity of the electrode may lead to an increased and prolonged activity of the Pt metal electrode. It can be operated at parameters where the local interfacial potential, and therefore the reaction rate, exhibits spatiotemporally inhomogeneous distributions. Examples are standing waves, travelling pulses and complex spatiotemporally oscillating patterns. The theoretical simulations were clearly confirmed by experimental observations and *vice versa*, as described below.

- A hidden negative differential resistance (HNDR) was deduced from the electrochemical impedance spectra near the onset of potential oscillations, while a manifest NDR appears to be responsible for the oscillations at higher potentials.

- Phase resetting (pulse advancement) and controlled pulse reversal on a Pt ring electrode during formic acid oxidation were strongly dependent on magnification and duration of external perturbation applied at one location of the ring.

- Spatiotemporal pattern sequence of the interfacial potential on a Pt ring WE was strongly dependent on the position of the RE. Inhomogeneous patterns (*Pulse* and *standing waves*) were observed when the RE was close to the WE due to negative nonlocal coupling, while the positive global coupling gave rise to homogeneous in-phase oscillations of the interfacial potential when the RE was sufficiently far away from WE. The influence of electrode inhomogeneities (defects) on pattern formation has been discussed.